SCHOOL OF COMPUTATION,
INFORMATION AND TECHNOLOGY

TECHNISCHE UNIVERSITÄT MÜNCHEN

Scientific thesis to achieve the degree
Master of Science in Communications Engineering

GNSS-Based Non-Cooperative Air Traffic Situational Awareness

Alberto Arana Ragel

DEPARTMENT OF ELECTRICAL ENGINEERING

SCHOOL OF COMPUTATION, INFORMATION AND TECHNOLOGY

TECHNISCHE UNIVERSITÄT MÜNCHEN

Scientific thesis to achieve the degree
Master of Science in Communications Engineering

GNSS-Based Non-Cooperative Air Traffic Situational Awareness

Author:	Alberto Arana Ragel
Work Supervisor:	Dr.-Ing. Alexandra Filip-Dhaubhadel Institute of Communications and Navigation - DLR
Academic Supervisor:	Dr.-Ing. Uwe Siart Chair of High-Frequency Engineering - TUM
Submission Date:	October 13, 2023

I confirm that this Scientific thesis to achieve the degree Master of Science in Communications Engineering is my own work and I have documented all sources and material used.

Munich, October 13, 2023 Alberto Arana Ragel

Acknowledgments

I would like to express my sincere gratitude to my colleagues and friends at the Institute for Communication and Navigation of the German Aerospace Center (DLR) for their invaluable contributions and for accompanying me throughout my journey as a master's student. I am particularly indebted to Dr.-Ing. Alexandra Filip-Dhaubhadel for her guidance, mentorship, and belief in my abilities. Your expertise and constant encouragement have been instrumental in the successful completion of this thesis, and your unbreakable strength has been a lesson of resilience that I will never forget.

I also want to thank the Technical University of Munich for providing me with the opportunity to pursue my master's degree and allowing me to conduct this thesis at DLR. I am deeply grateful to Dr.-Ing. Uwe Siart for fully supporting me whenever I needed it and for making the bureaucratic procedures as light as they can be.

To my friends, both here and back home, I extend my warmest thanks. You have always made my life amazing, and these months have been no exception. Your presence made the academic journey not only manageable but also enjoyable.

My family, who has been my source of strength throughout my life, deserves special mention. Your unwavering belief in my capabilities and constant encouragement have been the driving force behind my academic achievements. Thank you for always being there for me.

Lastly, I want to express my deepest gratitude to Carlota, my life partner and my everyday support. Your love and understanding during this demanding journey have been an invaluable source of strength. Having you by my side in the most challenging moments has not only sustained me but also enriched these months in countless ways.

I am truly grateful to all of you for being a part of this journey, and I couldn't have accomplished this without your support and encouragement.

Abstract

In this work, an initial feasibility assessment of a global navigation satellite system-based passive multistatic radar approach aimed at enabling non-cooperative air traffic situational awareness is performed. First, the bistatic case is studied, where the achievable theoretical detection performance study shows the need for a long integration time. The range and Doppler migration compensation approach needed to enable a high processing gain when using a long integration time in practice is therefore addressed and a multi-frame hybrid integration technique proposed. This target migration compensation approach merges both state-of-the-art single frame and multi-frame long integration techniques to enable long integration time processing for the air-to-air scenario of interest. More specifically, it corrects for the intra- and inter-frame range and Doppler migration components while allowing for different accelerations in each frame, inherently accounting for a geometry induced relative jerk. Preliminary simulation results show the effectiveness of the proposed approach. Building on this bistatic processing approach, the multistatic case is addressed. A reference domain for combining the bistatic results is defined and the transformation between domains is implemented such that to allow for the multistatic processing. Simulation results employing several satellites confirm the successful transformation and multistatic combination in the noise-free case. For the case with noise, the transformation is shown to give rise to some noise enhancement artifacts for specific geometries and remains the topic of future work.

Contents

Acknowledgments **v**

Abstract **vii**

List of Acronyms **xi**

1. Introduction **1**
1.1. Aim of this Work 3
1.2. Related Work 4
1.3. Contributions of this Work 5

2. Fundamentals **7**
2.1. Global Navigation Satellite Systems 7
2.2. Radar Systems 10
2.2.1. Bistatic Radar 11
2.2.2. Multistatic Radar 14
2.2.3. Ambiguity Function 14

3. GNSS-Based Passive Bistatic Radar **17**
3.1. Signal Synchronization 17
3.2. Cross-Ambiguity Function Evaluation 18
3.3. Long Integration Time 20
3.4. Migration Compensation 23
3.4.1. Single Frame Migration Compensation 24
3.4.2. Multi-Frame Migration Compensation 27

4. GNSS-Based Passive Multistatic Radar **35**
4.1. Multistatic Geometry 36
4.2. Implemented Approach 41

5. Conclusion and Future Work **51**

A. GNSS comparison **53**

B. Additional Results **57**

List of Figures **59**

List of Tables **61**

Bibliography **63**

List of Acronyms

A2A	air-to-air.
A2G	air-to-ground.
ADS-C	automatic dependent surveillance-contract.
ADS-B	automatic dependent surveillance-broadcast.
AF	ambiguity function.
ATC	air traffic control.
ATM	air traffic management.
AWGN	additive white Gaussian noise.
CAF	cross-ambiguity function.
CPI	coherent processing interval.
CZT	chirp-Z transform.
DAB	digital audio broadcasting.
DFT	discrete Fourier transform.
DLR	*Deutsches Zentrum für Luft- und Raumfahrt*.
DOA	direction of arrival.
DVB-S	digital video broadcast - satellite.
DVB-T	digital video broadcast - terrestrial.
FFT	fast Fourier transform.
FM	frequency modulated.
FrFT	fractional Fourier transform.
GNSS	global navigation satellite system.
GSs	ground stations.
IFFT	inverse fast Fourier transform.
IoO	illuminator of opportunity.
KT	Keystone transform.
LDACS	L-band digital aeronautical communication system.
LoS	line of sight.
NM	nautical miles.
PRI	pulse repetition interval.
PRN	pseudo-random-noise.
PSD	power spectral density.
PSR	primary surveillance radar.
RCS	radar cross section.
RPK	revenue passenger-kilometers.

Rx	receiver.
SAR	synthetic aperture radar.
SNR	signal-to-noise ratio.
SoO	signals of opportunity.
SSR	secondary surveillance radar.
TCAS	Traffic Alert and Collision Avoidance System.
TMC	target migration compensation.
TUM	Technical University of Munich.
Tx	transmitter.

1. Introduction

In the recent history of commercial air transport, there has been an increasing trend in the revenue passenger-kilometers (RPK), which has only been temporarily disrupted by major events or crises [1], with one of these events being the Covid-19 worldwide pandemic. However, with the RPK having already reached 88% of the maximum pre-Covid value by March 2023, an unprecedented demand in passenger air traffic is to be expected [2]. This forecast is depicted in Fig. 1.1, where it can be seen that the demand in air travel is expected to double by 2040.

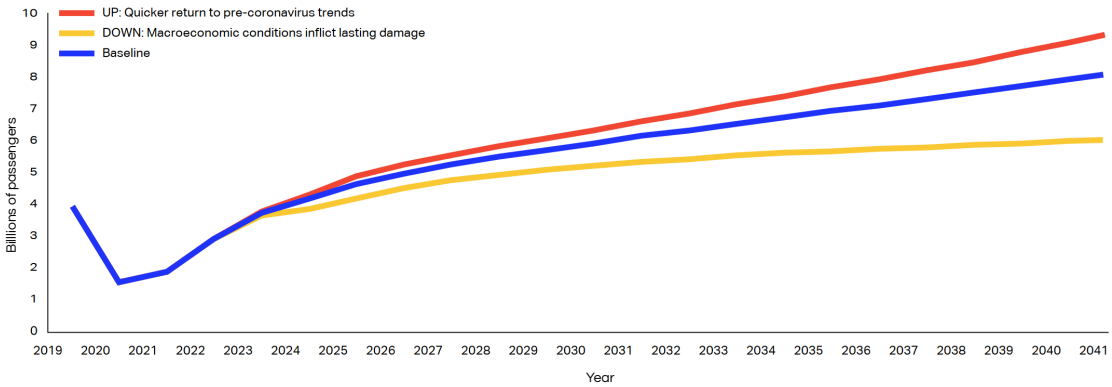

Figure 1.1.: Global air passengers per year forecast (adapted from [2]).

This increase in the amount of global air passengers inevitably entails a higher airspace traffic load with which the air traffic management (ATM) systems have to deal. This higher load, in turn, increases the risk of accidents in the air which, without a proper subsequent expansion of the ATM performance, could materialize into actual mid-air collisions.

Of special importance to the ATM system performance is the surveillance component. This provides the air traffic control (ATC) with surveillance services, allowing it to monitor flying aircraft. State-of-the-art surveillance is based on the secondary surveillance radar (SSR) and the primary surveillance radar (PSR). While the latter employs active radars to detect the aircraft non-cooperatively, the former system is a cooperative one. As such, it employs interrogations that aircraft should respond to in order to be identified. The ranges of these systems are 100 nautical miles (NM) for PSR and 250 NM for SSR [1]. A third surveillance component is brought by the automatic dependent surveillance-broadcast (ADS-B) service, in which aircraft broadcast their own global navigation satellite system (GNSS)-determined position through the ADS-B Out equipment. The ADS-B ground stations (GSs) are then able to gather these broadcast

messages and monitor the aircraft when flying within the coverage area, which extends to up to 250 NM [3].

Outside of the range of ground-based surveillance sensors, aircraft use ADS-B and Traffic Alert and Collision Avoidance System (TCAS) for mid-air situational awareness, whose ranges are 200 NM and 30 NM [4], respectively. If equipped with ADS-B In equipment, aircraft can receive other aircraft's ADS-B Out messages. Moreover, TCAS is based on the transponder interrogation and replies between aircraft, further enhancing the situational awareness and providing traffic and resolution advisories when potential collisions are detected [4]. This working principle is displayed in Fig. 1.2.

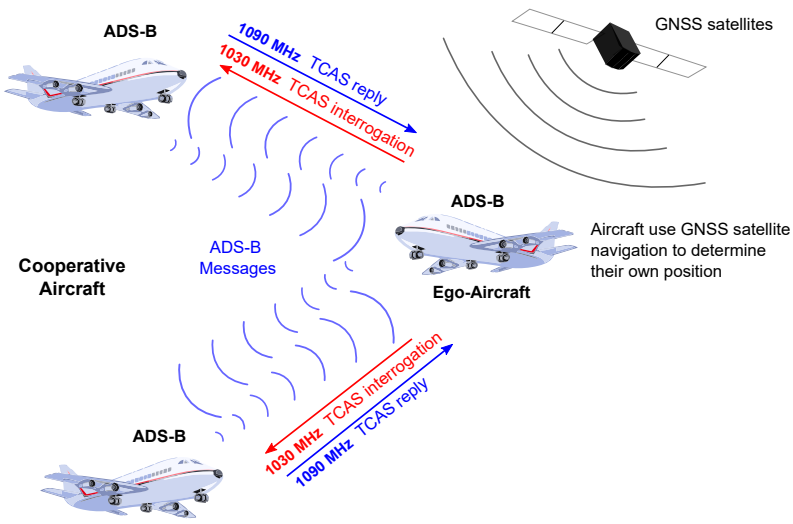

Figure 1.2.: State-of-the-art situational awareness in civil air traffic.

It can be therefore noted that outside the range of ground-based PSR and SSR, aircraft rely exclusively on cooperative systems, that is ADS-B and TCAS, in order to detect and avoid collisions with other aircraft. This is also the case in remote regions such as oceanic ones, where aircraft cannot be detected by ground-based surveillance systems [5]. Since these systems require all aircraft to be cooperative, they become ineffective in the case of transponder malfunction or sabotage. Another inherent problem given the aforementioned air traffic load increase is the further worsening of the situation concerning the 1090 MHz band. This frequency band is already very congested, being used for the SSR and the TCAS interrogation replies, as well as for the ADS-B broadcast messages. As such, an intended jamming of this band would lead to an outage of the situational awareness and collision avoidance systems. Furthermore, a failure in the transponder would incapacitate ADS-B and TCAS, leaving aircraft invisible to the ATC and non-detectable to other aircraft that might be flying nearby.

1.1. Aim of this Work

Motivated by the lack of a backup non-cooperative situational awareness system to be used in case of transponder malfunction or jamming of airplanes, the objective of this work is to propose a concept that would allow for such a component. However, since airborne radars are an unfeasible solution cost- and spectrum-wise, a non-trivial problem is presented. Given the aforementioned congestion of the 1090 MHz frequency band and the widely known demand of frequency spectrum, a solution based on an illuminator of opportunity (IoO) is considered instead. This would allow for an illuminator to be used for a purpose different than the one it was designed for. In particular, the navigation satellites that make up the different GNSS constellations are intended to be used as IoOs, with the GNSS signals transmitted by these satellites playing then the role of signals of opportunity (SoO). The proposed concept is depicted in Fig. 1.3, where the signals transmitted by the various GNSS satellites impinge on the non-cooperative aircraft generating reflections that are captured at the ego-aircraft. These reflected signals are the ones intended to be used for detecting the non-cooperative aircraft that may be flying in the proximity.

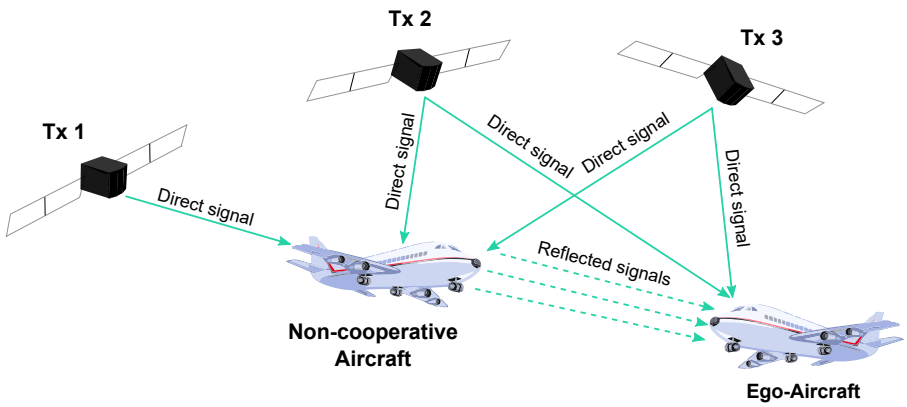

Figure 1.3.: GNSS-based non-cooperative situational awareness.

The advantages of employing the GNSS signals as SoO for this application are multifold. First off, a continuous global coverage is a major requirement for providing reliable situational awareness in remote regions. In this respect, it is known that every GNSS constellation simultaneously illuminates every point on the Earth surface with 4 to 8 satellites [6]. This also brings a major advantage in terms of spatial diversity. Additionally, the GNSS signals are already optimized for ranging purposes, being therefore well suited for radar applications. Lastly, their large bandwidth ensures enough resolution for aircraft detection purposes.

However, a major challenge also arises from the decision of employing the GNSS signals as SoO. To begin with, the GNSS technology relies on spread spectrum techniques, with the signal power spectral density known to be very low. This inherently results in very low power signal reflections off the non-cooperative aircraft.

Moreover, challenges also arise from the scenario of interest. As it can be seen in Fig. 1.3, all the components of the system are mobile, and, due to the low received power of the signals, a long integration time is needed in theory in order to gather enough energy to detect the aircraft. Nevertheless, the movement of the transmitter (Tx), receiver (Rx), and the target during the long integration time result in a dispersion of the target energy across multiple delay and Doppler cells. While the details of this phenomena will be addressed in more detail in Chapter 3, they are known to result in loss of the target signal-to-noise ratio (SNR). Given the aforementioned power restriction, this introduces the need for target migration compensation (TMC) techniques, which are aimed at recovering all the spread energy in a single point, therefore improving the SNR such that to be able to detect the aircraft. The study and implementation of these techniques are the cornerstone of this work.

1.2. Related Work

Non-Cooperative Surveillance Systems

In the air-to-ground (A2G) surveillance segment, there have been several research works aimed at providing backup non-cooperative surveillance services. Among these, the following are noted: [7] which takes advantage of the soon-to-be standardized L-band digital aeronautical communication system (LDACS) and the signals transmitted by its multiple GSs, [8] which uses the digital video broadcast - terrestrial (DVB-T) transmitters as IoO, and [9] which considers employing several radio frequency broadcasting sources, such as DVB-T, digital audio broadcasting (DAB), and frequency modulated (FM)-radio, as IoOs for surveillance purposes.

However, as already motivated before, a non-cooperative air-to-air (A2A) surveillance component has still not been considered. In addition to this, it should be noted that these research works only consider terrestrial-based IoOs, which is known to limit their usability for surveillance in the air due to their limited coverage.

GNSS Signals as SoO

GNSS signals have already been used as SoO for several applications such as: reflectometry for remote sensing of the Earth surface [10], passive synthetic aperture radar (SAR) imaging for Earth observation [11], imagery of ships [12], and surveillance [13]. The latter is of particular interest due to the similarity to the envisioned application presented in this work. There have been several research works focusing on the surveillance of different types of targets: a) maritime targets [6], [14]–[17], b) terrestrial targets [18], [19], and c) air targets [20]–[23]. Although the latter is similar to the envisioned application, all these works are intended to operate with ground-based and not with airborne Rxs. Since the aim of this work is to provide situational awareness for aircraft in the air, the aircraft need to carry an airborne Rx, realizing an A2A detection scheme. To the best of

the author's knowledge, GNSS signals have not yet been considered for A2A passive detection purposes.

1.3. Contributions of this Work

Given the previously mentioned challenges that arise from the use of GNSS signals as SoO in connection to the challenging radar geometry, a signal processing chain that implements the TMC techniques and maximizes the processing gain is needed. In this research work, an initial approach for developing a non-cooperative GNSS-based A2A situational awareness component is presented. First, an algorithm that processes the radar reflections from a single satellite is developed, and the associated passive bistatic radar detection capabilities studied and evaluated. This algorithm combines several state-of-the-art TMC techniques and extends them to achieve a higher degree of migration compensation for the scenario at hand. After the performance evaluation, the approach is further extended to allow for jointly processing the reflections from several satellites such that to allow for a passive multistatic radar. A centralized data fusion algorithm is then implemented for combining the results from several satellites and leveraging the diversity gain, realizing a centralized multistatic radar processing chain. The performance of both the bistatic and multistatic radar processing algorithms is tested with the help a radar simulator developed at the *Deutsches Zentrum für Luft- und Raumfahrt* (DLR).

Worth highlighting are the facts that the A2A non-cooperative surveillance concept presented here is novel and the signal processing chain employed considers the migration effects and the consequently needed TMC to an extent not considered in previous research works. The need for these high-order TMC techniques is specific to the scenario studied here.

Outline

In Chapter 2, the basics of GNSS and radar systems are presented. Furthermore, in Chapter 3 the GNSS-based passive detection concept is introduced and the implementation of two different signal processing approaches is addressed. The simulation results associated with the bistatic case are presented and analyzed. In Chapter 4 the latter approach is extended to a multistatic scenario, where several satellites are considered as IoOs and the resulting performance improvement is assessed. Lastly, in Chapter 5 the conclusion and some future work directions are presented.

2. Fundamentals

2.1. Global Navigation Satellite Systems

The acronym global navigation satellite system (GNSS) refers to a satellite navigation system able to provide global position information. It is composed of a constellation –a group of navigation satellites– and a ground network [24]. Moreover, the GNSS constellations ensure a continuous global coverage by illuminating every point on Earth by at least 4 and up to 8 satellites. There are currently 4 working GNSS systems operating in different frequency bands: GPS, Galileo, GLONASS, and Beidou-3 and the distribution of these bands can be seen in Fig. 2.1. Of special interest to this work are the navigation signals that these satellites transmit, which can be used as signals of opportunity (SoO). The signal characteristics of the different GNSS systems and frequency bands differ greatly from one another, thus a selection had to be made in terms of the most optimum candidate for the purpose of this work. In this respect, the E5 Galileo signals were selected for reasons exposed in the next subsection.

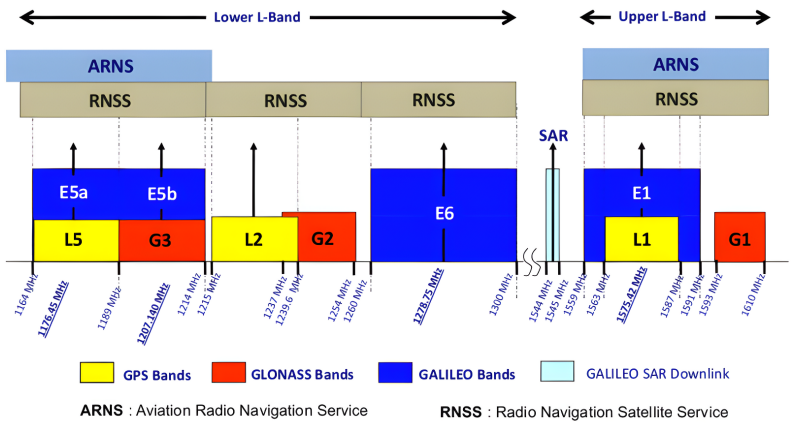

Figure 2.1.: GNSS frequency bands [25].

Galileo E5

Galileo is Europe's GNSS system, which started its development in 2003. This system provides services in three different frequency bands called E1, E5, and E6, each one of which has different signal-in-space characteristics. For this work, the Galileo E5 signals, which are centered at 1191.795 MHz, were selected as SoO. The reasons for this are multifold. The Galileo E5 band is separated in two subbands, E5a and E5b. These can be

used jointly to allow for a resolution higher than with any other available GNSS signal, while also enabling the highest power density flux that reaches the Earth surface. In addition, the quadrature components of the two subbands do not carry a navigation message, which implies that this data does not need to be decoded, simplifying the underlying signal processing [11]. A plot of the power spectral density (PSD) of the E5 signal can be seen in Fig. 2.2. Also, a detailed comparison of the different GNSS signal characteristics is presented in Appendix A. In the remainder of this subsection, the Galileo E5a/E5b signals generation and structure are detailed.

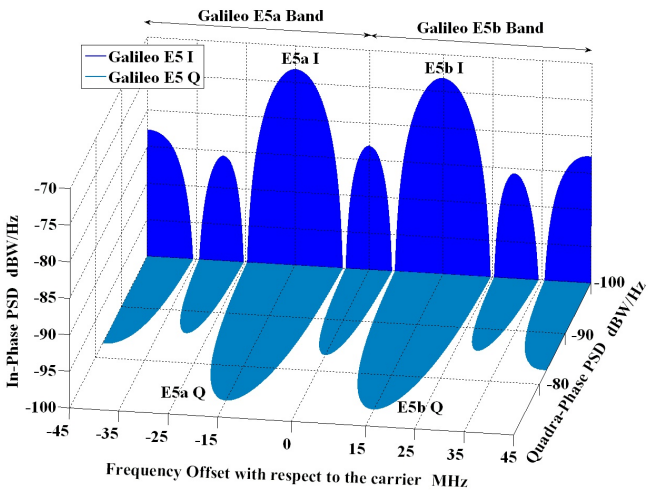

Figure 2.2.: PSD of the Galileo E5 signal [25].

The Galileo E5a/E5b signals follow a special tiered code structure which consists of a combination of two pseudo-random-noise (PRN) codes of different lengths and chip rates, and, therefore, of different potential unambiguous ranges and range resolutions. The generation of the code is carried out as depicted in Fig. 2.3, where N_s represents the dividend between the two codes chip rates: f_{cp}, which is the chip rate of the primary code, and f_{cs}, which represents that of the secondary code. The chips of both codes get combined, producing the new chips of the entire tiered code. With this structure, the secondary code modifies successive repetitions of the primary code, as shown in Fig. 2.4, therewith lengthening the period of the tiered code. The reason for employing this construction is enhancing the spatial period of the signal, thus increasing the unambiguous range [26].

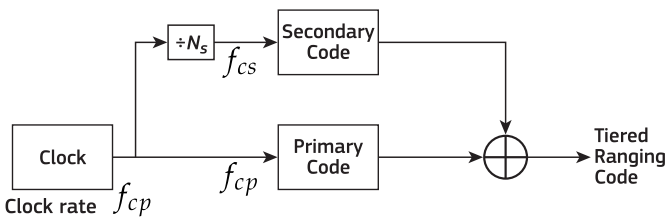

Figure 2.3.: Tiered code generation (adapted from[27]).

The secondary code chip duration is always equal to the primary code period, which means that each secondary code chip is combined with the respective entire primary code. The starting point of the chips of the secondary code are synchronized with the starting point of the primary code. The working principle can be therefore understood in the following manner: each chip of the secondary code shifts (or not) an entire repetition of the primary code. With this structure, the new period of the code is equal to that of the secondary code. This can be seen in more detail in Fig. 2.4.

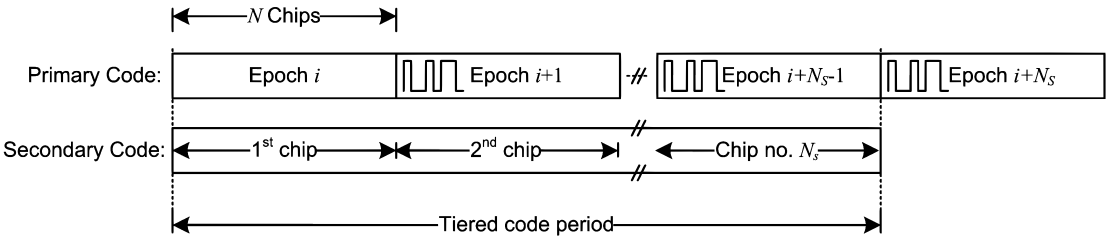

Figure 2.4.: Tiered code structure [27].

The parameters of the E5a/E5b primary and secondary codes are presented in Table 2.1. For simplicity, only the E5a signal is considered for the rest of this work. However, all the equations and algorithms introduced are valid for all GNSS signals. A simplified version of the E5a signal can be therefore expressed as

$$g(t) = C_{E5a\text{-}I} N_{E5a\text{-}I} cos(2\pi f_c t) + \mathrm{j} C_{E5a\text{-}Q} sin(2\pi f_c t) \ , \tag{2.1}$$

where $N_{E5a\text{-}I}$ represents the navigation data, the tiered ranging code of the in-phase component is $C_{E5a\text{-}I}$, $C_{E5a\text{-}Q}$ is the quadrature component code, f_c denotes the carrier frequency, and t is the continuous time. Accounting for the fact that only the quadrature component of the signal is of interest in this work, the in-phase component is omitted hereinafter. Disregarding the constant amplitude and phase terms, the E5a-Q signal can be then written as

$$g(t) = C_{E5a\text{-}Q} cos(2\pi f_c t) = SC_{E5a\text{-}Q}(t) PC_{E5a\text{-}Q}(t) cos(2\pi f_c t) = s(t) cos(2\pi f_c t) \ , \tag{2.2}$$

where $SC_{E5a\text{-}Q}(t)$ is the secondary code of the E5a-Q signal, and $PC_{E5a\text{-}Q}$ is the respective primary code.

Band	**Signal component**	**Tiered Code Period** ms	**Code length (in chips)**	
			Primary	**Secondary**
E5a	I	20	10230	20
	Q	100	10230	100
E5b	I	4	10230	4
	Q	100	10230	100

Table 2.1.: E5a/E5b code parameters.

Having detailed the basics of the Galileo E5 signals relevant to this work, the basics of radar systems and its key characteristics are presented next.

2.2. Radar Systems

A radar system is aimed at the detection of targets and the estimation of the target parameter by means of the reflections of electromagnetic waves off these targets in an area of interest. Provided a baseband transmitted signal, $s(t)$, the received reflected signal given the presence of a target at a range R can be defined as

$$r(t) = \alpha_r s(t - \tau(t)) \mathrm{e}^{\mathrm{j}2\pi f_c (t - \tau(t))} + \psi(t) \ , \tag{2.3}$$

which can be seen as an attenuated, delayed, and noisy version of the transmitted signal. In (2.3), α_r represents the overall attenuation coefficient, $\tau(t)$ denotes the time-dependent delay associated with the range to the target R, and $\psi(t)$ is the complex additive white Gaussian noise (AWGN). If the target of interest is moving at a constant relative velocity, $v_r = dR/dt$ the Doppler shift is defined as

$$\nu = -\frac{1}{\lambda}\frac{dR}{dt} = -\frac{1}{\lambda} v_r = -\frac{f_c}{c} v_r \ , \tag{2.4}$$

while the time-dependent delay $\tau(t)$ can be expressed as a function of the motion parameters as

$$\tau(t) = \tau_0 + \frac{v_r}{c} t = \tau_0 + \frac{-\nu}{f_c} t \ , \tag{2.5}$$

where τ_0 is the value of the delay $\tau(t)$ at $t = 0$ s. Using (2.4) and (2.5), (2.3) can be expressed as

$$r(t) = \alpha_r \mathrm{e}^{-\mathrm{j}2\pi f_c \tau_0} s\left(t - \left(\tau_0 - \frac{\nu}{f_c} t\right)\right) \mathrm{e}^{\mathrm{j}2\pi \nu t} \mathrm{e}^{\mathrm{j}2\pi f_c t} + \psi(t) \ . \tag{2.6}$$

From (2.6) it can be seen how the physical parameters of the target are embedded in the reflected signal, principle exploited by radar systems to extract the delay and the Doppler shift of the targets.

Although the radar working principle is common to all radar systems, there can be different waveforms and operation modes, different platforms, and different antenna configurations. In regards to the latter classification method, three types of radar systems can be distinguished: monostatic, bistatic, and multistatic radars, as depicted in Fig. 2.5. While in a monostatic radar system the transmitter (Tx) and receiver (Rx) are collocated, in a bistatic radar system the Tx and Rx are physically separated from one another by a considerable distance called the baseline. Intuitively, a multistatic radar system consists of multiple independent bistatic radar links realized by all the possible combinations between the available Txs and Rxs. In this case the different aspect angles provide a spatial diversity advantage and increase the probability of target detection, given that a centralized processing is performed.

The attention is now turned to the bistatic radar case in particular.

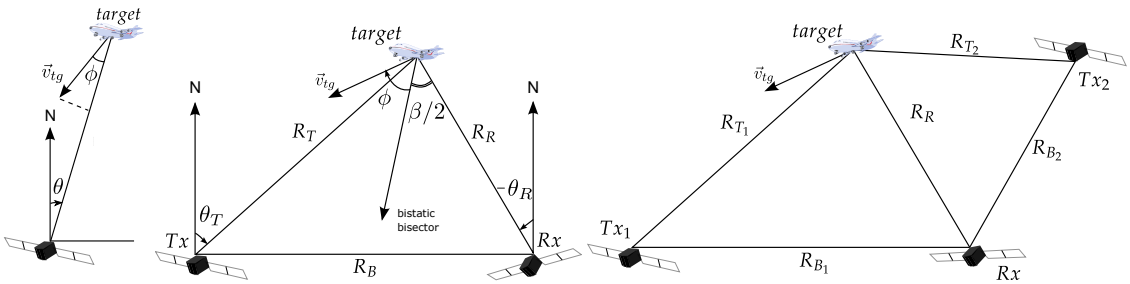

(a) Monostatic (b) Bistatic (c) Multistatic

Figure 2.5.: Radar types.

2.2.1. Bistatic Radar

A bistatic radar system consists of spatially separated Tx and Rx both illuminating an area of interest. This is also the scenario of interest to this work: a generic GNSS satellite takes the role of the Tx, while the airborne Rx is mounted on the ego-aircraft. The target(s) are the non-cooperative aircraft that could be flying nearby. This is shown in Fig. 2.5b. In order to properly understand the implications of this scenario, the geometry, its repercussions on the signal model, as well as the link budget capabilities will be studied next.

First, the preliminary link budget obtained as a result of the scenario and the selected SoO is analyzed. The tool employed for this assessment is the bistatic radar equation, which is obtained from [28] and expressed as

$$R_{R_{\max}} = \sqrt{\frac{P_T G_T G_R \lambda^2 \sigma T_{\text{int}}}{(4\pi)^3 R_T^2 \text{SNR}_{\text{out,req}} L_R k_B T_0 F_R}}\,, \tag{2.7}$$

where P_T represents the transmit power, G_T and G_R denote the Tx and Rx antenna gains, respectively, λ represents the signal wavelength, σ is the target radar cross section (RCS), T_{int} denotes the integration time, R_T is the Tx-to-target range, L_R represents the Rx losses, while F_R denotes the Rx noise figure. Also, k_B the Boltzmann constant, T_0 is the standard temperature, and $\text{SNR}_{\text{out,req}}$ is the required output signal-to-noise ratio (SNR) associated with the selected bistatic detection performance, and obtained as

$$P_d = P_{fa}^{\frac{1}{1+\text{SNR}_{\text{out,req}}}}\,, \tag{2.8}$$

where P_d represents the probability of detection and P_{fa} is the probability of false alarm. (2.8) holds when considering a Swerling 1 target model and a square-law detector.

Next, the bistatic geometry is analyzed in Fig. 2.6. Here, the scenario of interest can be seen with the two aircraft –ego-aircraft and non-cooperative aircraft– representing the Rx and target, respectively, in addition to the Tx which is a GNSS satellite. As previously mentioned, all the components are mobile and therefore have their own velocities. For this work, non-accelerating components are considered. Three line of sight (LoS) vectors are depicted in Fig. 2.6. The three ranges of interest, which can be expressed as the

absolute value of the LoS vectors, are: 1) the baseline range, i.e., the range between Tx and Rx, $\left|\overrightarrow{R_{B_i}(t)}\right|$, 2) the Tx-to-target range, $\left|\overrightarrow{R_{T_i}(t)}\right|$, 3) and the target-to-Rx range, $\left|\overrightarrow{R_R(t)}\right|$. The subscript i denotes the ith satellite. Moreover, the velocities of the Tx, Rx, and target are denoted as $\vec{v}_R$, $\vec{v}_{T_i}$, and $\vec{v}_{tg}$, respectively.

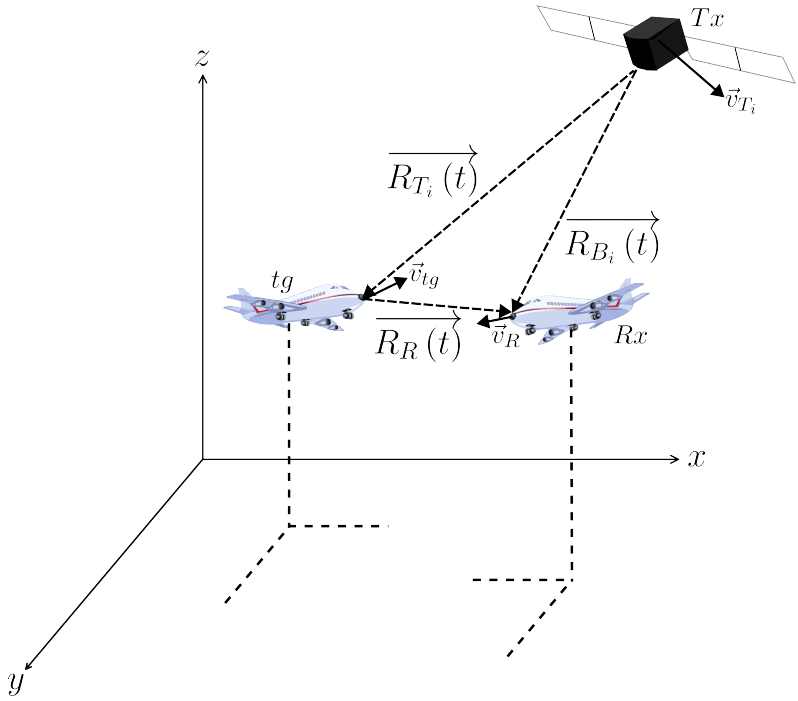

Figure 2.6.: Bistatic geometry.

From the geometry depicted in Fig. 2.6, the expressions for the three ranges of interest can be derived using a Taylor expansion. To allow for this, the subscript $_0$ denotes a magnitude relative to the time instant $t = 0$ s, while the ranges $R_{T_i,0}$, $R_{B_i,0}$, and $R_{R,0}$ represent the absolute value of the respective LoS vectors at $t = 0$ s, i.e., $\left|\overrightarrow{R_{T_i}(0)}\right|$, $\left|\overrightarrow{R_{B_i}(0)}\right|$, and $\left|\overrightarrow{R_R(0)}\right|$. For simplicity, only the components up until the third degree are considered. The Tx-to-target range can therefore be expressed as

$$\begin{aligned}\left|\overrightarrow{R_{T_i}(t)}\right| = R_{T_i,0} + t\frac{\overrightarrow{R_{T_i,0}}}{R_{T_i,0}}\left(\vec{v}_{tg} - \vec{v}_{T_i}\right) + t^2\left(\frac{\left(\vec{v}_{tg} - \vec{v}_{T_i}\right)^2}{2R_{T_i,0}} - \frac{\overrightarrow{R_{T_i,0}}^2}{R_{T_i,0}^2}\frac{\left(\vec{v}_{tg} - \vec{v}_{T_i}\right)^2}{2R_{T_i,0}}\right) \\ + t^3\left(\frac{\left(\vec{v}_{tg} - \vec{v}_{T_i}\right)^3}{2{R_{T_i,0}}^2}\frac{\overrightarrow{R_{T_i,0}}^3}{R_{T_i,0}^3} - \frac{\overrightarrow{R_{T_i,0}}}{R_{T_i,0}}\frac{\left(\vec{v}_{tg} - \vec{v}_{T_i}\right)}{2{R_{T_i,0}}^2}\right) + \text{higher order terms}\,.\end{aligned} \tag{2.9}$$

The baseline range is similarly expressed as follows

$$\begin{aligned}\left|\overrightarrow{R_{B_i}(t)}\right| &= R_{B_i,0} + t\frac{\overrightarrow{R_{B_i,0}}}{R_{B_i,0}}\left(\vec{v}_R - \vec{v}_{T_i}\right) + t^2\left(\frac{\left(\vec{v}_R - \vec{v}_{T_i}\right)^2}{2R_{B_i,0}} - \frac{\overrightarrow{R_{B_i,0}}^2}{R_{B_i,0}^2}\frac{\left(\vec{v}_R - \vec{v}_{T_i}\right)^2}{2R_{B_i,0}}\right) \\ &+ t^3\left(\frac{\left(\vec{v}_R - \vec{v}_{T_i}\right)^3}{2{R_{B_i,0}}^2}\frac{\overrightarrow{R_{B_i,0}}^3}{R_{B_i,0}^3} - \frac{\overrightarrow{R_{B_i,0}}}{R_{B_i,0}}\frac{\left(\vec{v}_R - \vec{v}_{T_i}\right)}{2{R_{B_i,0}}^2}\right) + \text{higher order terms}\ .\end{aligned} \tag{2.10}$$

Lastly, the target-to-Rx range takes the form

$$\begin{aligned}\left|\overrightarrow{R_R(t)}\right| &= R_{R,0} + t\frac{\overrightarrow{R_{R0}}}{R_{R,0}}\left(\vec{v}_{tg} - \vec{v}_R\right) + t^2\left(\frac{\left(\vec{v}_{tg} - \vec{v}_R\right)^2}{2R_{R,0}} - \frac{\overrightarrow{R_{R0}}^2}{{R_{R,0}}^2}\frac{\left(\vec{v}_{tg} - \vec{v}_R\right)^2}{2R_{R,0}}\right) \\ &+ t^3\left(\frac{\left(\vec{v}_{tg} - \vec{v}_R\right)^3}{2R_{R,0}^2}\frac{\overrightarrow{R_{R0}}^3}{R_{R,0}^3} - \frac{\overrightarrow{R_{R0}}}{R_{R,0}}\frac{\left(\vec{v}_{tg} - \vec{v}_R\right)}{2R_{R,0}^2}\right) + \text{higher order terms}\ .\end{aligned} \tag{2.11}$$

These equations are used throughout this report as the starting point for several explanations in Chapter 3 regarding the migration effects and the target migration compensation (TMC). Moreover, they also play an important role for the manipulation of the scenario geometry needed for the multistatic processing in Chapter 4.

Reflected Signal Model

In this section, the bistatic reflected signal model is developed when starting from (2.3). Here it is important to underline the fact that the reflected signal, being dependent on the evolution of the delay with respect to time, is inherently dependent on the motion of the scenario. Moreover, as stated before, non-accelerating components are considered in this work. However, the different aspect angles vary along the integration time, inducing a relative acceleration. As such, (2.3) has to be extended to account for this geometry-induced acceleration. For this, the delay of the reflected signal, $\tau(t)$, has to be redefined. It can be expressed as

$$\tau(t) = \frac{\left|\overrightarrow{R_{T_i}(t)}\right| + \left|\overrightarrow{R_R(t)}\right|}{c} = \frac{R_i(t)}{c} = \frac{R_{i0}}{c} + \frac{v_{r,0}}{c}t + \frac{a_{r,0}}{2c}t^2 = \tau_0 + \frac{v_{r,0}}{c}t + \frac{a_{r,0}}{2c}t^2\ , \tag{2.12}$$

where c represents the speed of light in the atmosphere and τ_0, ν_0, and $a_{r,0}$ represent the delay, Doppler shift, and acceleration at $t = 0$ s, respectively.

If a constant relative acceleration is assumed, (2.3) can be expressed as

$$\begin{aligned}r(t) &= \alpha_r s(t - \tau(t))\mathrm{e}^{\mathrm{j}2\pi f_c(t-\tau(t))} + \psi(t) = \\ &= \alpha_r \mathrm{e}^{-\mathrm{j}2\pi f_c \tau_0} s\left(t - \left(\tau_0 - \frac{\nu_0}{f_c}t + \frac{a_{r,0}}{2c}t^2\right)\right)\mathrm{e}^{\mathrm{j}2\pi\nu_0 t}\mathrm{e}^{\mathrm{j}2\pi f_c t} \\ &\quad \times \mathrm{e}^{-\mathrm{j}2\pi\frac{a_{r,0}}{2\lambda}t^2} + \psi(t)\ ,\end{aligned} \tag{2.13}$$

which represents the reflected signal off one target of a signal originating from one satellite. The relative acceleration, however, can also vary in practice along the integration

time. This effect is called jerk and can be critical in some scenarios. Nevertheless, this effect is not considered for the analytical study. With the help of (2.7) the attenuation coefficient α_r is defined as

$$\alpha_r = \sqrt{\frac{P_T G_T G_R \lambda^2}{(4\pi)^3 R_T^2 R_R^2 L_T L_R}} \zeta \,, \tag{2.14}$$

where ζ denotes the complex reflection coefficient of the target which is directly related to the RCS, $\sigma = |\zeta|$.

2.2.2. Multistatic Radar

A multistatic radar system consists of multiple independent bistatic radar links, with the different aspect angles providing a spatial diversity advantage and therefore increasing the probability of target detection. This is represented in Fig. 2.5c. The latter point limits however the possibility of a fully coherent approach since the different aspect angles of viewing the target will result in the reflected signals reaching the ego-aircraft through the different paths having different phases. Moreover, it is important to note that, from a signal processing perspective, the joint processing associated with a multistatic radar operation distinguishes it from a collection of bistatic radars which function independently in a decentralized way. However, there are several ways of performing this joint processing, with different signal processing gains associated, in relation to the amount of information that these are able to employ. The four types of data fusion are: radio signal fusion, video signal fusion, plot fusion and track fusion, with the degree of spatial coherence required for these methods being shown in Fig. 2.7.

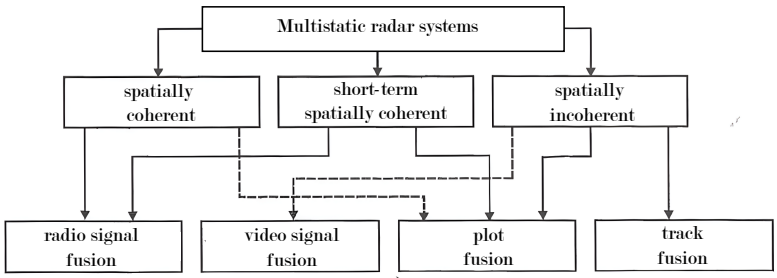

Figure 2.7.: Multistatic radar types (adapted from [29]).

2.2.3. Ambiguity Function

In radar signal processing and waveform analysis, the ambiguity function (AF) is a fundamental tool. It allows for characterizing the resolution capabilities of a signal by demonstrating how effectively it can discriminate between objects at various ranges and velocities. Its analytical expression can be written as

$$|\chi(\tau,\nu)|^2 = \left| \int_{-\infty}^{\infty} s(t) s^*(t-\tau) \mathrm{e}^{-\mathrm{j}2\pi\nu t} dt \right|^2 \,, \tag{2.15}$$

where the superscript * represents the conjugate operation. The AF is essentially a two-dimensional function that measures the auto-correlation of a signal with delayed and Doppler shifted versions of itself. The AF can be also understood as the time and frequency response of the matched filter operation to a noise free point target of unit amplitude [30].

Next, the AF of the Galileo E5a signal is analyzed. It is known [31] that the complete E5 signal delivers a range resolution of 8 m, while the E5a and E5b components have each a range resolution of 14.7 m, respectively. This can be confirmed as follows. Starting from the signal bandwidth of the Galileo E5a/E5b signals $B = 20.46$ MHz, the delay resolution of the signal results $\tau_{\text{res}} = 1/B = 48.88$ ns. This in turn allows to obtain the range resolution as $R_{\text{res}} = c\tau_{\text{res}}/2 = 14.7\,\text{m}$, matching the value of the literature. This can also be confirmed when analyzing Fig. 2.8, with the AF of the E5a signal shown in Fig. 2.8a and the corresponding zero-Doppler AF cut shown in Fig. 2.8b. The software used to generate these plots is the open source GNSS signal generator from [32]. The

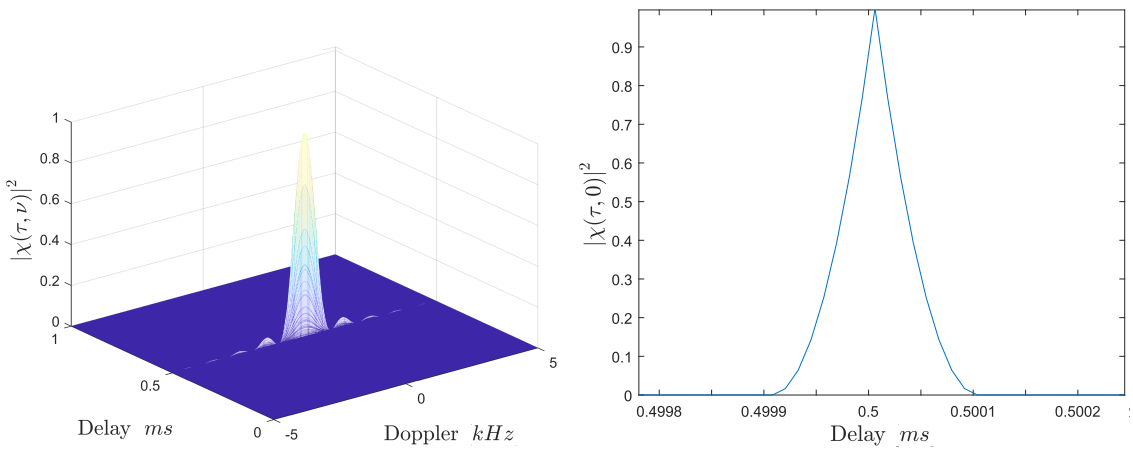

(a) AF **(b)** Zero-Doppler AF cut

Figure 2.8.: AF of the Galileo E5a signal.

width of the AF main lobe confirms the theoretical result obtained before.

Directly connected to the AF is the cross-ambiguity function (CAF). In particular, the CAF computes the correlation between the radar received signal $r(t)$ and delayed and Doppler shifted versions of the transmitted one $s(t)$. Accordingly, the CAF takes the form

$$|\chi_{\text{CAF}}(\tau,\nu)|^2 = \left| \int_0^T r(t) s^*(t-\tau)\, \mathrm{e}^{-\mathrm{j}2\pi\nu t} dt \right|^2 , \tag{2.16}$$

where T represents the coherent processing interval (CPI). It is a function of the time delay and Doppler shift, mapping to the fast-time/slow-frequency domain. This operation is critical in radar applications including target tracking, radar interferometry, and radar signal processing, with the latter being the subject of interest to this work.

In radar signal processing it is usually of interest to analyze the received signal in the dual domains, which are a critical framework for analyzing and interpreting radar

data. These are the fast time-slow time, fast frequency-slow time, fast frequency-slow frequency, and fast time-slow frequency. The fast-time dimension represents the shorter time scale and deals with the quick variations in radar signals generated by changes in target distance or range, whereas the slow-time dimension records changes in target behavior over longer time intervals. The equivalent frequency domains explore the spectrum components of this fast/slow variations. The most commonly employed domain in signal analysis is the fast-time/slow-frequency domain, corresponding to the as delay-Doppler domain. This domain allows for detecting and tracking the range-velocity characteristics of the targets. In Fig. 2.9, the fast Fourier transform (FFT)/inverse fast Fourier transform (IFFT) operations connecting the different domains are depicted.

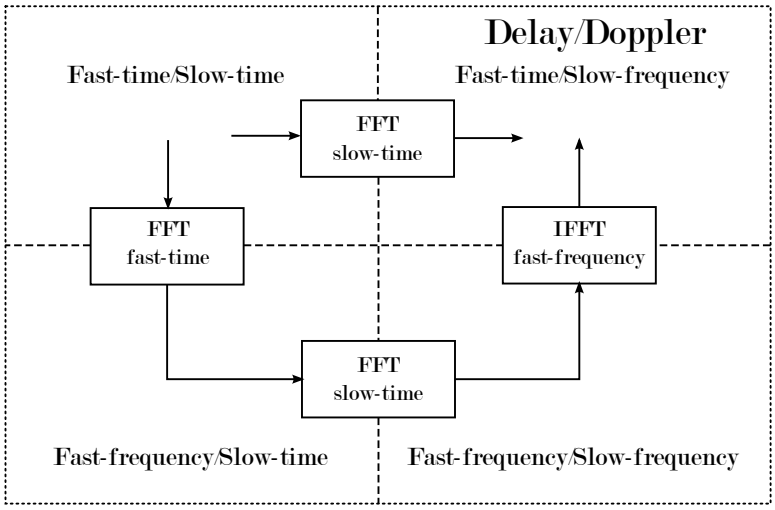

Figure 2.9.: Dual domains (adapted from [7]).

These domains will become relevant when looking into more detail at the migration compensation techniques.

3. GNSS-Based Passive Bistatic Radar

In Section 1.1 the low signal power density and the fast changing geometry were introduced as the main challenges of the envisioned concept. These entail that in order to achieve reliable global navigation satellite system (GNSS)-based passive detections, the signal processing gain has to be maximized, thus aiming at leveraging all the available information. This leads to the necessity of achieving a coherent signal processing of the received signal. For this, it is essential that the transmitter (Tx) and receiver (Rx) components are synchronized before performing matched filtering for the acquisition of the cross-ambiguity function (CAF). In order for the signal synchronization to be achieved, the direct signal traveling through the baseline line of sight (LoS) vector undergoes a synchronization process, with which a noise-free replica of the direct signal is generated. This reference signal is further on used in the matched filtering stage, after which the range compressed data matrix is obtained. The migration compensation is then applied to this range compressed data in order to obtain the refocused bistatic delay/Doppler map. A block diagram of the overall system processing is shown in Fig. 3.1.

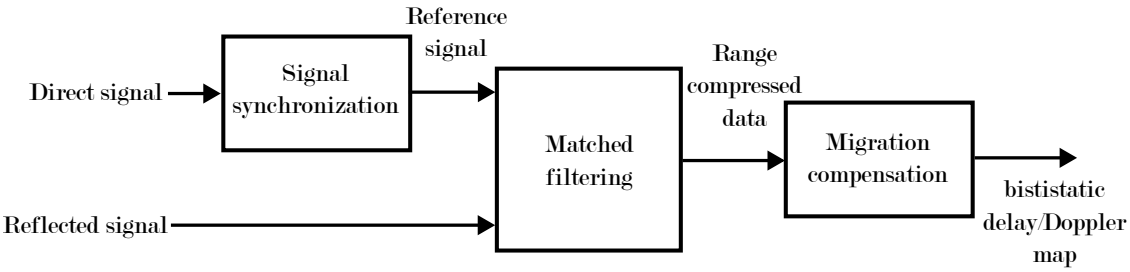

Figure 3.1.: Bistatic system block diagram.

3.1. Signal Synchronization

When referring to signal synchronization it is worth distinguishing between the spatial, time, and phase synchronization dimensions that this entails [33]. To begin with, the spatial synchronization is guaranteed when both Tx and Rx are simultaneously illuminating the surveillance area of interest. By comparison, time synchronization is associated with a common time reference and is needed to ensure that no drift arises between the Tx and Rx clocks. This is crucial for enabling highly precise time, and consequently also range, measurements. Lastly, phase synchronization is needed to ensure that no phase error is introduced in the received signal as a result of the

frequency deviation between the Tx and Rx local oscillators. The lack of phase and time synchronization inherently arise from the use of different hardware equipment —oscillators and clocks— in the Tx and in the Rx and require dedicated measures [28].

When employing GNSS satellites as illuminator of opportunity (IoO), spatial synchronization can be ensured by only considering those satellites that during the time of processing are illuminating the target. This can be determined at the initial acquisition. Since time and phase synchronization are affected by clock slippage and oscillator phase drift, a dedicated signal synchronization stage is needed in order to provide the time and phase reference and ensure time and phase synchronization. This signal synchronization stage aims to account for the effects that would arise from an imperfect time and phase synchronization and eliminate them by providing a reference noise-free replica of the direct signal to the matched filtering stage. The detail of this signal synchronization stage has been addressed in previous works like [34] and will therefore not be addressed further here.

3.2. Cross-Ambiguity Function Evaluation

In this research work, the CAF is employed to evaluate the performance of the developed approaches. The CAF is the outcome of the matched filtering block in Fig. 3.1 and it undergoes thereafter the target migration compensation (TMC) stages. As it was stated before, the CAF essentially illustrates how correlated two signals are. As it can be seen in Fig. 3.1, the noise-free local replica of the direct signal is the one used for performing the matched filtering operation. This means that the differences in delay and Doppler shift between both signals that will be inferred from the CAF will have to be interpreted as those in comparison with the noise-free replica of the direct signal. This fact can be derived analytically, being the range, and inherently delay, and Doppler shift related to the LoS vectors denoted in Fig. 2.6 as the following equations expose:

$$R_{D_i}(t) = \left|\overrightarrow{R_{T_i}(t)}\right| + \left|\overrightarrow{R_R(t)}\right| - \left|\overrightarrow{R_{B_i}(t)}\right| \ , \tag{3.1}$$

$$\begin{aligned} \nu_{D_i} &= -\frac{1}{\lambda}\frac{\partial R_{D_i}(t)}{\partial t} = -\frac{1}{\lambda}\left(\frac{\partial\left(\left|\overrightarrow{R_{T_i}(t)}\right| + \left|\overrightarrow{R_R(t)}\right| - \left|\overrightarrow{R_{B_i}(t)}\right|\right)}{\partial t}\right) \\ &= \nu_{T_i} + \nu_R - \nu_{B_i} \ . \end{aligned} \tag{3.2}$$

This also partially eliminates the migration effects related to the baseline motion [14].

However, the computation of the CAF is known to be a highly demanding operation. Due to this high computational complexity, an efficient method for obtaining the CAF has to be considered. The previously described fast-time/slow-time domain can be used as an alternative framework for evaluating and analyzing the CAF.

Batches Algorithm

Mirroring the work in [7], the Batches algorithm is decided to be used due to its high efficiency [35]. This algorithm is based on the reformatting of both the reference and the received signals previous to the matched filtering operation. The received signal is first divided in smaller data segments, often referred to as "batches", whose size has to be decided in relation to the maximum detectable delay and Doppler, while the reference signal undergoes a similar process. The segmentation process can be seen in Fig. 3.2. The continuously transmitted signal, $s(t)$, is comprised of N_{seg} continuous batches of L_{seg} samples each, with its time span representing the pulse repetition interval (PRI), denoted by T_r. Additionally, these are zero-padded with $L_{\max} = \tau_{\max} fs$ samples, where f_s is the sampling frequency. Once the transmit signal is divided into these segments, they are organized as columns within a transmit matrix denoted as S. Moreover, the reflected signal, $r(t)$, is partitioned into N_{seg} segments, each with a duration of $T_r + \tau_{\max}$. These segments are organized such that there is an overlap of $L_{\max}$ samples between any two adjacent segments, forming the columns of a receive matrix called R. This overlap is essential to ensure that the mth transmit segment corresponds to the mth receive segment. To allow for this rearrangement, the duration of the reflected signal must be $T + \tau_{\max}$. The pulse duration is calculated as $T_r = L_{\text{seg}}/f_s$, while the integration time is determined as $T = L_{\text{seg}} N_{\text{seg}}/f_s$. As a second step, matched filtering is performed along each batch for obtaining the range compressed data.

It is worth highlighting that this algorithm actually computes an approximation of the CAF, and therefore suffers from a signal-to-noise ratio (SNR) loss, whose extent can be adjusted by modifying the parameters of the signal reformatting.

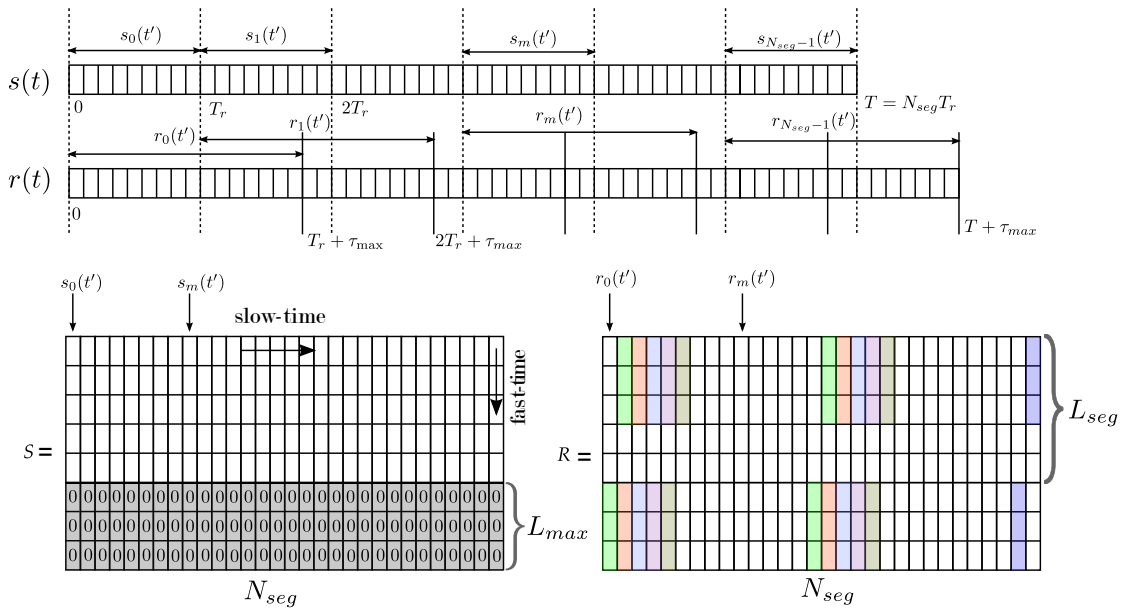

Figure 3.2.: Batches algorithm signal segmentation (adapted from [7]).

The approximation to the CAF can be then expressed as

$$\chi^{b}_{\mathrm{CAF}}\left(\tau,\nu\right) \approx \mathrm{e}^{-\mathrm{j}2\pi\nu T_r/2} \sum_{m=0}^{N_{\mathrm{seg}}-1} \mathrm{e}^{-\mathrm{j}2\pi\nu m T_r} \int_0^{T_r+\tau_{\max}} r_m\left(t'\right) s^*_m\left(t'-\tau\right) dt' \,, \tag{3.3}$$

where t' represents the fast time dimension, $t' \in \left[0, T_r + \tau_{\max}\right]$, and m is the slow time index across the batches, i.e., the batch index is $m \in \left[0, N_{\mathrm{seg}} - 1\right]$. The delay and Doppler shift are defined as $0 \leq \tau \leq \tau_{\max}$ and $-\nu_{\max} \leq \nu < \nu_{\max}$, with $\nu_{\max}$ given as

$$\nu_{\max} < \frac{1}{2T_r} = \frac{f_s}{2L_{\mathrm{seg}}} \,. \tag{3.4}$$

3.3. Long Integration Time

Given the limitations of using the low transmit power GNSS signals as signals of opportunity (SoO), the aim is to maximize the signal processing gain and therefore improve the target output SNR. It is known that the relation between the input and output SNRs is given by the processing gain as

$$\mathrm{SNR}_{\mathrm{out}} = \mathrm{SNR}_{\mathrm{in}} \times G_p \,, \tag{3.5}$$

where the processing gain can be expressed as a function of the coherent processing interval (CPI), T, and the bandwidth of the signal, B, as

$$G_p = TB \,. \tag{3.6}$$

As such, the signal processing gain G_p can be increased by increasing the integration time or the bandwidth [36]. Since the bandwidth is fixed by the IoO of choice, the remaining option is to increase the integration time.

Nevertheless, the use of a long integration time leads to: 1) a higher computational load, and 2) a dispersion of the target energy along several delay/Doppler cells as a result of the movement of the target during the CPI. These migration effects of particular interest to this work are addressed in more details in Section 3.3.

Link Budget Analysis

Before that, however, it is of interest to assess how long of an integration time is needed in practice. To allow for this, the attention is now turned to the link budget. For this evaluation, the bistatic radar equation in (2.7) is used, together with the input parameters in Table 3.1. This analysis has been performed in a previous work and is not a part of this work. The results are however included here for completion. A fully coherent integration along the complete integration time is assumed. The computation assumes a probability of detection of $P_d = 0.75$ and a probability of false-alarm of $P_{\mathrm{fa}} = 10^{-4}$. The results showing the maximum detection range $R_{R_{\max}}$ versus the radar cross section (RCS) are depicted in Fig. 3.3 for two integration times of 4 s and 8 s, respectively.

Table 3.1.: Link budget parameters.

Parameter	Value
Carrier frequency f_c	1176.45 MHz
Transmit power P_T	50 W
Transmit antenna gain G_T	15 dBi
Tx to target range R_T	23210 km
Receive antenna gain G_R	15 dBi
Rx loss L_R	2 dB
Rx noise figure F_R	1 dB
Standard temperature T_0	290 °K
Rx Bandwidth B	20.46 MHz
RCS σ	100 m^2

From Fig. 3.3, it can be seen that, already in the fully coherent case, the maximum detection range is very limited for the selected parameters. The maximum detection range is a key performance indicator for the envisioned application, since a larger maximum detection range would allow for a longer reaction time for the aircraft. The needed performance in maximum detection range R_R defines then the required integration time T_{int}. This is understood from the relation between the output SNR and the integration time in (3.5). However, it should be noted that the results shown in Fig. 3.3 only account for the quadrature component of half a transmission band, and also for a single satellite. This means that the maximum detection range can be further increased by considering more satellites or transmission bands. Nevertheless, the extent of the energy dispersion provoked by the long time integration needs to be assessed for the geometries considered in this work.

To be able to analyze the migration effects associated with a long integration time, a scenario of interest has been defined. This is described as follows: the Galileo GSAT0211 satellite with PRN E02 is the Tx of opportunity while the Rx and the target are two aircraft, both flying at an altitude of 2.6 km and with a constant airspeed of 300 km/h. The target and Rx, with an initial separation between them of $R_R = 1.6$ km, are approaching each other, and their trajectories, extracted from a previous *Deutsches Zentrum für Luft- und Raumfahrt* (DLR) measurement campaign, are parallel to each other, being separated by 160 m. The simulation is carried out with a DLR radar simulator where a constant RCS along the entire integration time is assumed and the same noise generator seed is employed in all the simulations such that to allow for comparability between different approaches. The noise power, as well as the mean attenuation power $|\alpha|^2$, in addition to the target input SNR are given in Table 3.2. The noise power is obtained from the Rx parameters provided in Table 3.1.

Table 3.2.: Input SNR parameters.

Parameter (in dB)	Mean $\lvert\alpha\rvert^2$	Noise power	SNR_{in}
Value	-187.3	-129.9	-57.4

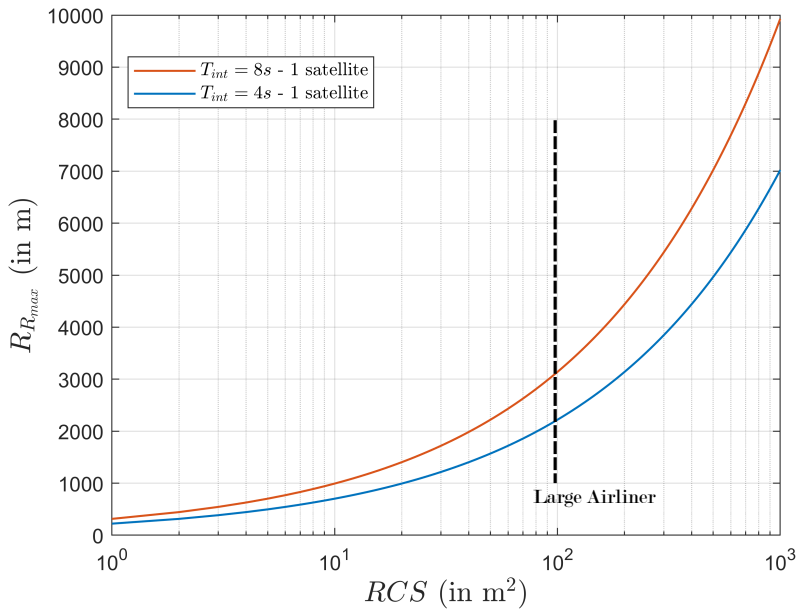

Figure 3.3.: Max detection range vs. RCS for 1 satellite and 2 different integration times.

Next, the batches algorithm is used to evaluate the CAF for the aforementioned scenario. To this end, a $T_{\text{int}} = 8$ s is assumed and both a noise-free and a noisy scenario are considered. As depicted in Fig. 3.1, the reference signal obtained from the synchronization stage is used as the transmit signal for the matched filtering stage. The results are shown in Fig. 3.4. From Fig. 3.4a it can be seen that integrating for 8 s without taking into account the movement of the target, Tx and Rx during this time leads to migration effects in both delay and Doppler.

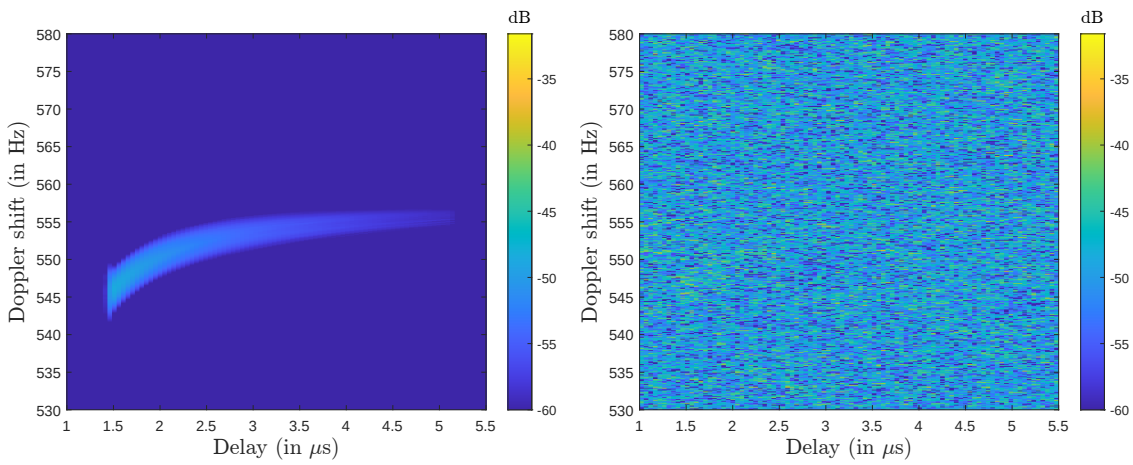

(a) Noise-free **(b)** Noisy scenario

Figure 3.4.: Delay/Doppler plot, single frame processing, uncompensated, $T_{\text{int}} = 8$ s.

The underlying migration effects and jerk-induced curvature are clearly seen in the single frame uncompensated noise-free Delay/Doppler map in Fig. 3.4a. These results

motivate the need for TMC techniques, as the migration effects spread the signal energy along multiple delay and Doppler cells, resulting in a loss of the target output SNR. As depicted in Fig. 3.4b, the signal remains buried under the noise, making the detection of the target impossible.

Migration Effects

A good understanding of the origin of these migration effects is needed in order to allow for their compensation. Since such an air-to-air (A2A) GNSS-based passive radar scenario has not yet been considered in the literature, the extent of the migration components that this application gives rise to are yet to be explored. In a first step, state-of-the-art TMC techniques are applied to the scenario of interest and the applicability of these algorithms to the case studied is analyzed.

Nevertheless, state-of-the-art TMC techniques are defined for more static scenarios that the one of interest, which allows the researchers to consider a constant relative acceleration, i.e., no jerk, along the entire integration time. As a result, any jerk component can be neglected. Following this assumption, the reflected signal model in (2.13) can be introduced in (3.3). Manipulating the expression further, the fast-frequency/slow-time representation of the CAF is assumed to take the form [7]:

$$\begin{aligned}
\mathbf{X}_{\text{ffst}}(f', m) &= \alpha \mathrm{e}^{-\mathrm{j}2\pi f_c \tau_0} \mathrm{e}^{\mathrm{j}2\pi \nu_0 m T_r} \mathrm{e}^{-\mathrm{j}2\pi f_c \frac{a_0}{2c} m^2 T_r^2} S_m\left(f' - \nu_0\right) S_m^*(f') \mathrm{e}^{-\mathrm{j}2\pi f' \tau_0} \mathrm{e}^{\mathrm{j}2\pi f' \frac{\nu_0}{f_c} m T_r} \\
&\quad \times \mathrm{e}^{-\mathrm{j}2\pi f' \frac{a_0}{2c} m^2 T_r^2} + \Psi_m(f') S_m^*(f') \ , \\
&= \alpha \mathrm{e}^{-\mathrm{j}2\pi f_c \tau_0} S_m\left(f' - \nu_0\right) S_m^*(f') \mathrm{e}^{-\mathrm{j}2\pi f' \tau_0} \underbrace{\mathrm{e}^{\mathrm{j}2\pi \nu_0 \left(\frac{f'+f_c}{f_c}\right) m T_r}}_{\text{linear range walk}} \underbrace{\mathrm{e}^{-\mathrm{j}2\pi \frac{a_0}{2\lambda} \left(\frac{f'}{f_c}\right) m^2 T_r^2}}_{\text{range curvature}} \underbrace{\mathrm{e}^{-\mathrm{j}2\pi \frac{a_0}{2\lambda} m^2 T_r^2}}_{\text{Doppler migration}} \\
&\quad + \Psi_m(f') S_m^*(f') \ ,
\end{aligned} \tag{3.7}$$

where f' represents the fast frequency, i.e., the frequency along the batches, and S_m is the Fourier transform of the mth segment of $s(t)$.

In (3.7), the range walk and the Doppler migrations are both linear effects, while the range curvature is a quadratic one. The three underlined exponential components are the ones responsible for the energy dispersion in the case where no jerk arises and should consequently be compensated by the TMC stages.

3.4. Migration Compensation

In order to maximize the signal processing gain and ensure a maximum output SNR, a refocusing of the spread energy is carried out. To this end, the migration components present in (3.7) have to be fully compensated for, ensuring that at the end of the processing all the target energy is concentrated in a single delay-Doppler cell. The techniques to do so have been widely studied in the literature [15], [37], [38]. Aligning with [7], the delay-Doppler cell of interest is defined as the one correspondent to the

initial point in time, i.e., that which describes the geometry status at $t = 0$ s. From (3.7) it is clear that the TMC has to be performed in both axes.

3.4.1. Single Frame Migration Compensation

In a first stage, the passive detection of a non-cooperative aircraft at the ego-aircraft is attempted when employing one single IoO, i.e., one single Galileo satellite, which essentially realizes a bistatic radar. As an initial assessment of the scenario capabilities and challenges, the approach developed in [7] is mirrored. This implementation was developed for an air-to-ground (A2G) scenario, where the L-band digital aeronautical communication system (LDACS) ground stations (GSs) were used as IoO, and the reflections were captured at one or several Rx GSs. This approach therefore considered a much more static scenario, where the only motion present was that of the target. As such, the algorithm does not consider a jerk component and assumes a constant relative acceleration throughout the entire integration time. It is therefore of interest to assess the performance of this algorithm in a geometry that changes much faster, where higher-order migration components could play an important role.

Since in [7] only first and second-order migration components are considered, the fast-frequency/slow-time response is assumed to resemble the one in (3.7). There, it is proven that these effects can be fully compensated with a three-step TMC processing based on the Keystone transform (KT).

The KT is a well-known technique used in synthetic aperture radar (SAR) and passive radar applications to perform an axis rescaling. In this work, the KT is used to perform a rescaling of the slow-time axis, with the purpose of decoupling the fast-frequency domain from the slow-time one, since the nature of the data format entails a coupling between the two axes. Different approaches can be used to perform the KT, with the chirp-Z transform (CZT) implementation having gained a lot of interest due to its high efficiency and good performance in comparison to the other approaches [39]. Consequently, similarly as in [7] the CZT is also used here to allow for the slow-time axis rescaling.

The range curvature and range walk migration effects present in (3.7) are each compensated using a CZT-based KT operation, with the same slow time axis rescaling factor $m' = m\sqrt{f_c/(f_k + f_c)}$, where f_k represents the discrete fast-frequency. In between the two KT operations, the Doppler migration is compensated for using a phase term multiplication factor, which takes the form

$$\Phi_{\text{Dopp,single}} = \mathrm{e}^{\mathrm{j}2\pi \frac{\widehat{a}_0}{2\lambda} m^2 T_r^2} \,, \tag{3.8}$$

where $\widehat{a}_0$ represents an estimate of the geometry-induced relative acceleration. This estimate can be obtained either by applying a fractional Fourier transform (FrFT) in the fast-frequency/slow-time domain as in [40], or, alternatively, using a bank of filters matched to a range of accelerations and applying the entire processing chain for each possible estimate, as assumed in [6]. This multiplication should be carried out in the

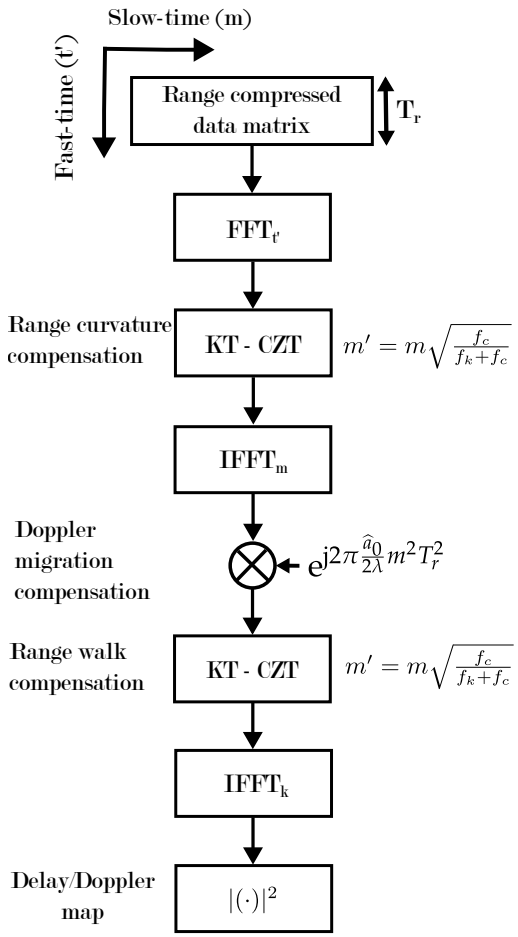

Figure 3.5.: Single frame migration compensation processing approach.

fast-frequency/slow-time domain, and hence an inverse fast Fourier transform (IFFT) operation along the slow-frequency axis is needed after the first KT operation and before the Doppler migration compensation. Lastly, the second KT is applied to correct fo the range walk, following which an IFFT operation along the fast-frequency is used to recover the delay/Doppler, i.e., fast-time/slow-frequency domain. The complete processing chain for this single frame approach is depicted in Fig. 3.5. In the final compensated delay/Doppler map the target energy is ideally accumulated at the delay/Doppler cell associated with the start of the CPI.

Next, it is of interest to evaluate the performance of this single frame approach for the simulated scenario introduced before. As presented before, an estimate of the geometry-induced relative accelerations is needed for the processing. For this estimation, the evolution of the acceleration along the entire integration time has to be analyzed, which is depicted in Fig. 3.6. In this plot, it can be clearly seen that the relative acceleration of the scenario is not constant, but rather has a high variation along the integration time. The jerk-induced curvature from Fig. 3.4a can then be understood as a result of this variation. Assuming $\hat{a}_0 = 0.24$ m/s^2, defined as a compromise value along

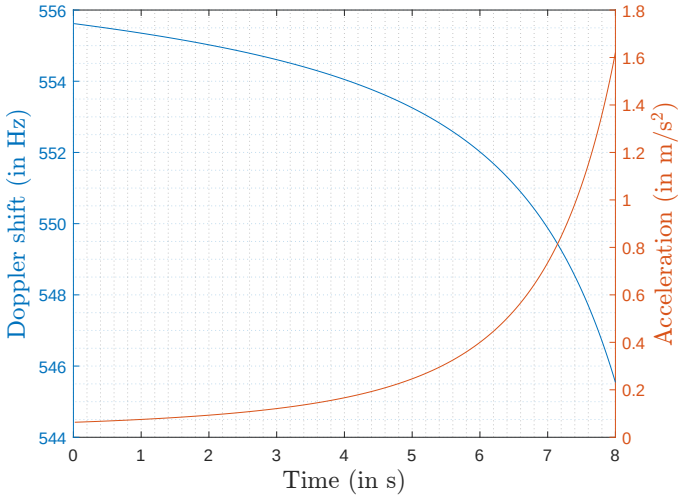

Figure 3.6.: Doppler shift and relative acceleration for the simulated geometry.

the acceleration span, and using the single frame migration compensation approach in Fig. 3.5, the compensated result in Fig. 3.7 is obtained. As it can be seen, a large part of the target energy is brought back to the initial point, as desired. Nonetheless, since the actually varying acceleration is not accounted for, part of the energy remains dispersed among the adjacent delay/Doppler cells, resulting in an 8.6 dB peak power loss when compared to the ideal case. The comparison of the output SNR to the ideal case is shown in Table 3.3. The ideal case corresponds to the fully coherent single frame approach where the energy would be fully compensated. As motivated already by Fig. 3.4a, the jerk-induced energy dispersion prevents the migration compensation to perform correctly. As shown in Fig. 3.7, there is some leftover target energy dispersion that worsens the detection performance.

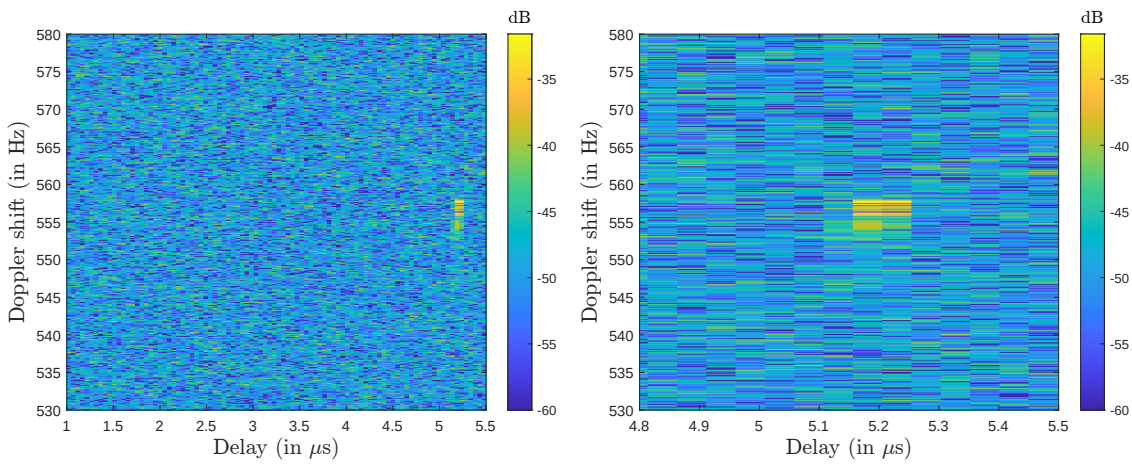

(a) Delay/Doppler plot **(b)** Delay/Doppler zoomed-in plot

Figure 3.7.: Delay/Doppler plots, single frame processing, compensated, $T_{\text{int}} = 8$ s.

Moreover, due to the highly dynamic geometry considered and the long time integra-

Table 3.3.: Single frame approach SNR performance.

Parameter (in dB)	Mean $\lvert\alpha\rvert^2$	$\mathrm{SNR}_{\mathrm{in}}$	Noise power
Ideal	-23	24.74	-47.74
Single frame	-31.61	16.13	-47.74

tion needed in practice, the RCS can not be considered coherent in a real scenario. This entails that a fully coherent processing of the entire integration time is not realizable, and an alternative is consequently searched for.

3.4.2. Multi-Frame Migration Compensation

One way to address the challenges associated with the single frame fully coherent processing approach is to perform a multi-frame hybrid processing instead. This means implementing an algorithm that combines both coherent and non-coherent signal processing stages. For this purpose, a multi-frame approach is proposed in which the non-coherent combination of multiple coherently integrated and compensated shorter frames is pursued, as also developed in [15] for the GNSS-based passive maritime surveillance application.

This approach divides the range compressed data matrix into N_f shorter ones, which are hereinafter referred to as frames. The partitioned fast-time/slow-time matrix corresponding to frame n can be denoted as

$$\mathbf{X}^n_{\mathrm{ftst}}\left[t', m\right] = \mathbf{X}_{\mathrm{ftst}}\left[t', [0 + (n-1)T_f : m : nT_f - 1]\right] \ , \tag{3.9}$$

where $0 \leq n \leq N_f - 1$, and m is redefined as $0 \leq m \leq T_f/T_r - 1$. In (3.9), the data is assumed to be already discretized. The objective is now to apply the single frame fully coherent approach to the individual frames and non-coherently combine them afterwards.

As a result, the fast-frequency/slow-time version of $\mathbf{X}^n_{\mathrm{ftst}}\left[t', m\right]$ can now be assumed to resemble the one in (3.7), with the new slow time being now dependent on both the slow-time index m and frame index n. Omitting the noise component for simplicity, the equivalent of (3.7) for one frame when accounting for the multi-frame framework can be consequently rewritten as

$$\mathbf{X}^n_{\mathrm{ffst}}\left[k, m\right] = \alpha^n_{k,m} \mathrm{e}^{\mathrm{j}2\pi\nu_0\left(\frac{f_k+f_c}{f_c}\right)\left(mT_r+nT_f\right)} \mathrm{e}^{-\mathrm{j}2\pi\frac{a_0}{2\lambda}\left(\frac{f_k}{f_c}\right)\left(mT_r+nT_f\right)^2} \times \mathrm{e}^{-\mathrm{j}2\pi\frac{a_0}{2\lambda}\left(mT_r+nT_f\right)^2} \ . \tag{3.10}$$

From (3.10), it can be seen that the migration components now depend on both the m and n indexes. This expression is central to understanding the migration effects that occur within a frame, i.e., those depending on m, hereinafter referred to as intra-frame migration, as well as the ones that occur from frame to frame, that is, those relative to n, that are further referred to as inter-frame migration.

In regards to the frame duration, several important considerations arise. The coherency of the RCS is one of the main restrictions imposed on the duration of a frame, since the

RCS must be constant within the entire frame. Moreover, since the fast-frequency/slow-time response is now assumed to be approximated by (3.7), it must be ensured that no jerk arises within a frames, i.e., the relative acceleration within a frame is constant. Furthermore, a smaller frame duration would inherently allow for a lower computation complexity. Nevertheless, shorter frames inherently lead to a lower integration gain due to their shorter CPI. Additionally, a shorter CPI also entails a lower Doppler resolution [28]. As a result, the frame size selection can be seen as a trade-off between the RCS coherency and intra-frame migration requirements, and the lower signal processing gain and Doppler resolution. Since the maximization of the integration gain is key to the performance of the approach, it is decided that the frame duration should be maximized while obeying the RCS and intra-frame jerk restriction. With this in mind, the frame duration is chosen to be $T_f = 0.5$ s. The resulting uncompensated delay/Doppler map in a noise-free case for the same scenario analyzed before is depicted in Fig. 3.8.

After the partitioning, each of the frames are individually processed with the intention of eliminating the intra-frame migration effects. As such, the single frame processing depicted in Fig. 3.5 is applied to each of the frames. Assuming that both range and Doppler migration effects are successfully compensated for, the following fast-frequency/slow-time expression for the nth frame should apply

$$\mathbf{X}^{n}_{\text{ffst,c}}[k,m] = \alpha^{n}_{k,m} \mathrm{e}^{-\mathrm{j}2\pi f_k \tau_{0,n}} \mathrm{e}^{\mathrm{j}2\pi \nu_{0,n} m_n T_r} \ , \tag{3.11}$$

where $\tau_{0,n}$ represents the initial delay of the nth frame, $\nu_{0,n}$ is the Doppler at the beginning of the nth frame, and $\alpha^{n}_{k,m} \approx \alpha \mathrm{e}^{-\mathrm{j}2\pi f_c \tau_{0,n}} S_m(f_k - \nu_{0,n}) S^*_m(f_k)$.

Nevertheless, since the aim is to refocus the target energy to the starting point of each frame, the resulting delay-Doppler cell which contains the energy is different for each of the frames This can also be seen in (3.11), as the compensated result for each of the frames depends on their initial delay and Doppler values, which for a mobile scenario would be different in each frame. This effect can be confirmed from Fig. 3.9, where the result of the intra-frame migration compensation is depicted for a noise-free simulation and the same parameters considered before.

This brings up the need for a second processing stage that aims to align these contributions to the begining of the CPI. This extra stage aligns the target energy of each of the frames to the inital point of the first frame, hence bringing all the target energy back to the start of the integration time.

To achieve the inter-frame migration compensation, the displacement of each frame in delay and Doppler have to be analytically evaluated. Firstly, the delay inter-frame migration component $\Delta\tau_n$ is derived by means of a Taylor expansion, as done in [15], as follows

$$\Delta\tau_n = \tau_{0,n} - \tau_0 = \tau_0 - \frac{\nu}{f_c} n T_f + \frac{\widehat{a}_{0,n}}{2c_0} n^2 T_f^2 - \tau_0 = -\frac{\nu}{f_c} n T_f + \frac{\widehat{a}_{0,n}}{2c_0} n^2 T_f^2 \ , \tag{3.12}$$

with $\nu = \left[-N_{\text{seg,f}}/2 : N_{\text{seg,f}}/2 - 1\right] \times 1/\left(T_r N_{\text{seg,f}}\right)$ denoting the entire Doppler domain and $N_{\text{seg,f}} = N_{\text{seg}}/N_f$ being the number of segments in a frame.

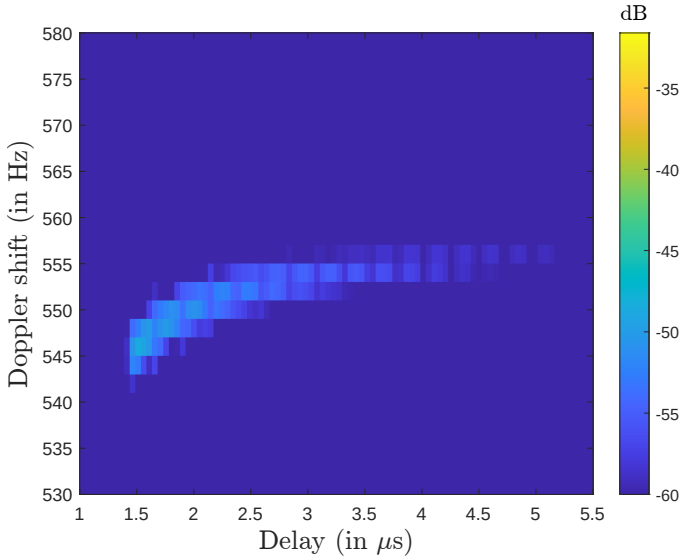

Figure 3.8.: Delay/Doppler plot, multi-frame processing, noise-free, uncompensated, $T_{\text{int}} = 8$ s, $T_f = 0.5$ s, sat. E02.

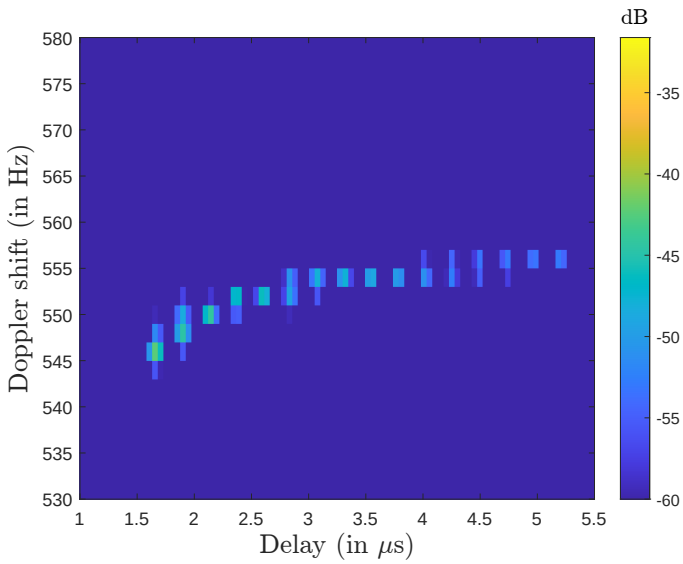

Figure 3.9.: Delay/Doppler plot, multi-frame processing, noise-free, intra-frame migration compensation only, $T_{\text{int}} = 8$ s, $T_f = 0.5$ s, sat. E02.

Secondly, the Doppler inter-frame migration component $\Delta\nu_n$ can be obtained as

$$\Delta\nu_n = \nu_{0,n} - \nu_0 = \dot{\nu}_{0,n} n T_f = -\frac{\widehat{a}_{0,n}}{\lambda} n T_f \ , \tag{3.13}$$

where $\dot{\nu}_{0,n}$ denotes the first derivative of $\nu_{0,n}$, i.e., the Doppler rate of change in the nth frame.

In order to compensate for these spread factors, a multiplication by a phase term in line with (3.12) and (3.13) is introduced in the processing. The multiplication factor

accounting for the inter-frame Doppler migration takes the form

$$\Phi_{\text{Dopp,n}} = \mathrm{e}^{-\mathrm{j}2\pi\Delta\nu_n m T_r} \ , \tag{3.14}$$

while the one that compensates the inter-frame delay migration is given as

$$\Phi_{\text{delay,n}} = \mathrm{e}^{\mathrm{j}2\pi\Delta\tau_n f_k} \ . \tag{3.15}$$

The compensation by these two factors is performed in the same way as with (3.8) and follows the same principles. The term in (3.14) is to be applied in the fast-frequency/slow-time domain, while for the subsequent multiplication by (3.15) a fast Fourier transform (FFT) to the slow-time axis has to be performed beforehand.

Once the inter-frame migration has been compensated, the data must be brought to an adequate format before the non-coherent combination. In this respect, all frames are returned to the fast-time/slow-frequency domain to allow for the delay/Doppler analysis.

Lastly, in a final step the compensated and aligned delay/Doppler maps associated with the different frames are non-coherently combined as

$$\left|\mathbf{X}_{\text{ftsf}}(t',\nu)\right|^2 = \sum_{n=0}^{N_f-1} \left|\mathbf{X}^n_{\text{ftsf}}(t',\nu)\right|^2 \ . \tag{3.16}$$

The resulting multi-frame migration compensation approach is depicted in Fig. 3.10.

It is now of interest to evaluate the performance of the multi-frame hybrid integration approach.

Constant Relative Acceleration

To begin with, it is assumed that a constant relative acceleration along all the frames can be considered, i.e., $\widehat{a}_{0,n} = \widehat{a}_0$, $\forall n$, $0 \leq n < N_f - 1$.

The result obtained when using the multi-frame approach with $T_f = 0.5$ s and assuming a constant $\widehat{a}_0 = 0.24$ m/s^2 in each frame is shown in Fig. 3.11. It can be seen that assuming a constant relative acceleration is not optimum, as the jerk that arises from frame to frame is representative enough to produce an energy spread and therefore lead to SNR loss. As a consequence, this relative jerk has to be accounted and compensated for. The resulting output SNR along the ideal and the single frame processing results is presented in Table 3.4. The reduced signal processing gain due to the hybrid processing in comparison to the fully coherent one is clearly seen.

Varying Relative Acceleration

Motivated by the limitations of the state-of-the-art algorithms when applied to the scenario of interest, the approach above is extended such that to consider a possible jerk and mitigate the resulting energy dispersion. To allow for this, the migration compensation routine is modified to account for different accelerations from frame to

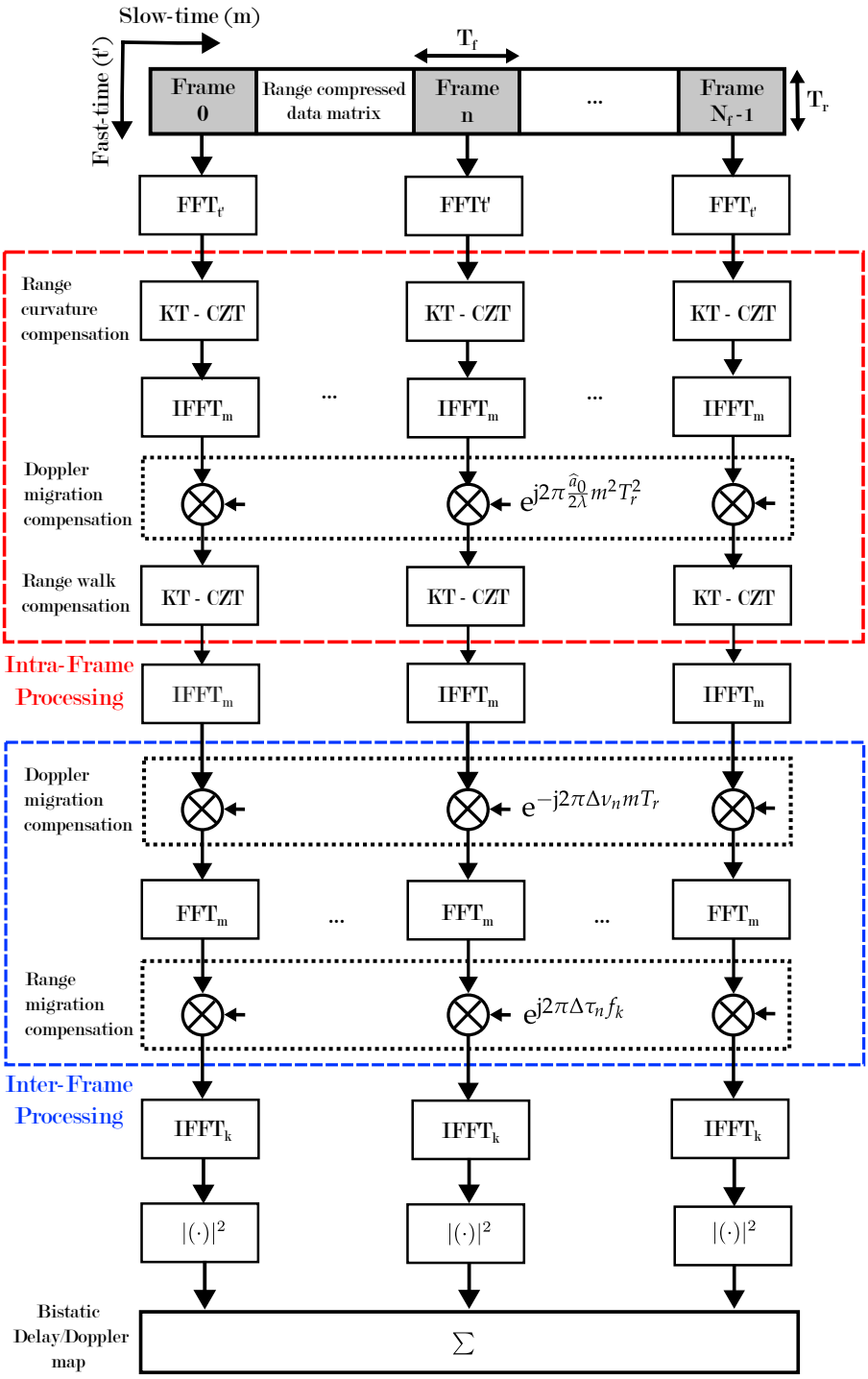

Figure 3.10.: Multi-frame migration compensation processing approach.

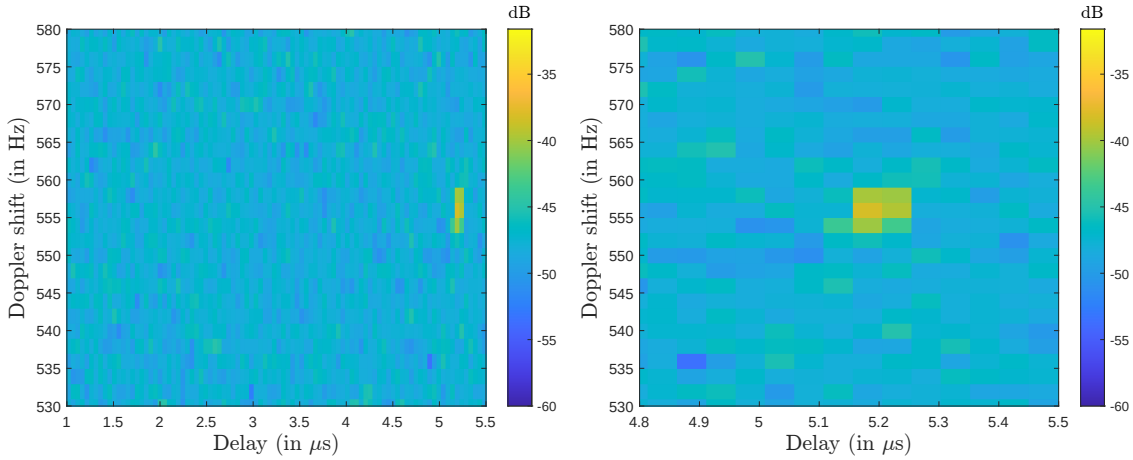

(a) Delay/Doppler plot **(b)** Delay/Doppler zoomed-in plot

Figure 3.11.: Delay/Doppler plots, multi-frame processing, $T_{\text{int}} = 8$ s, $T_f = 0.5$ s, $\widehat{a}_0 = 0.24$ m/s^2, sat. E02.

Table 3.4.: Constant acceleration multi-frame approach SNR performance.

Parameter (in dB)	Mean $\lvert\alpha\rvert^2$	Noise power	SNR_{in}
Ideal	-23	-47.74	24.74
Single frame	-31.61	-47.74	16.13
Multi-frame $\widehat{a}_{0,n} = \widehat{a}_0$	-38.25	-47.8	9.55

frame. The relative acceleration estimate considered in each frame, $a_{0,n}$, now models the acceleration history from the reference frame up to the nth frame. This is implemented by taking the mean of the accelerations of all frames up to the nth frame, with $a_{0,n}$ denoting the assumed constant acceleration in frame n, which is analytically described as

$$a_{0,n} = \frac{1}{n+1} \sum_{j=0}^{n-1} a_{0,j} \,. \tag{3.17}$$

Allowing for a varying acceleration from frame to frame inherently accounts for a relative jerk component, if this is to arise.

Next, the migration compensation performance of the newly proposed approach when compared to the other two approaches is evaluated. The novel approach is expected to fully compensate the migration and refocus all the energy to the delay/Doppler at the start of the integration time. The delay/Doppler map when using the multi-frame approach and accounting for the true acceleration in each frame is seen in Fig. 3.12. To decouple the impact of the target migration from other performance degradation effects, a perfect acceleration estimation, i.e., $\widehat{a}_{0,n} = a_{0,n}$ is assumed.

The results confirm that, as expected, accounting for the varying acceleration from frame to frame enables a full refocusing of the target energy at the correct delay/Doppler

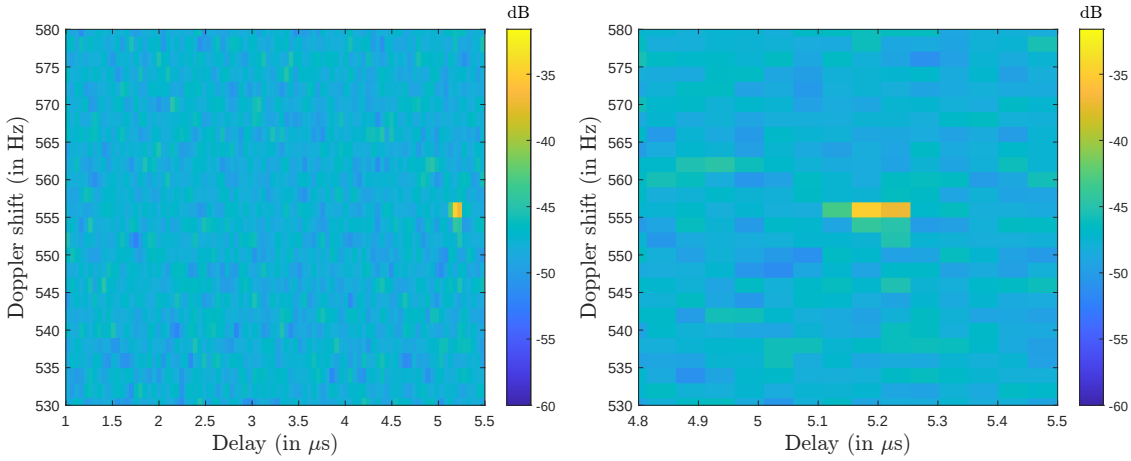

(a) Delay/Doppler plot **(b)** Delay/Doppler zoomed-in plot

Figure 3.12.: Delay/Doppler plots, multi-frame processing, $T_{\text{int}} = 8$ s, $T_f = 0.5$ s, $\widehat{a}_{0,n} = a_{0,n}$ m/s^2, sat. E02.

cell. This improvement leads to an increase of 3.4 dB in the processing gain when compared to the case where $\widehat{a}_{0,n} = \widehat{a}_0$. Moreover, it is worth highlighting that, although the peak power difference between the proposed multi-frame and the ideal fully coherent single frame approach remains representative, a further increase in the multi-frame integration gain is to be expected when either employing a longer illumination time, or considering further frequency bands and/or satellites. This peak power difference is a result of the reduced integration gain when pursuing non-coherent frame integration. A comparison between the output SNR obtained in each case is shown in Table 3.5.

Table 3.5.: Variable acceleration multi-frame approach SNR performance.

Parameter (in dB)	Mean $\lvert\alpha\rvert^2$	Noise power	SNR_{in}
Ideal	-23	-47.74	24.74
Single frame, $\widehat{a}_0$	-31.61	-47.74	16.13
Multi-frame, $\widehat{a}_{0,n} = \widehat{a}_0$	-38.25	-47.8	9.55
Multi-frame, $\widehat{a}_{0,n} = a_{0,n}$	-34.84	-47.8	12.96

It is clear that the multi-frame approach which considers a variable acceleration from frame to frame performs better than the one neglecting all jerk components. Moreover, it has a much lower computation complexity than the single frame case. This is then selected as the algorithm best suited for the envisioned application. Lastly, comparing the single and multi-frame approaches it can be noted that the former one, while enjoying lower discretization losses, is more sensitive to parameter mismatches and jerk components due to the high Doppler resolution, as it can be seen when comparing Fig. 3.7 to both Fig. 3.11 and Fig. 3.12. The multi-frame approach, however, has a lower Doppler resolution and is therefore less sensitive to mismatches. It is nonetheless affected by higher parameter discretization losses. Accordingly, and accounting for the

target RCS fluctuations in practice, extending the single frame approach to account for a jerk component would only bring a limited improvement in practice, at the expense of an even higher computation complexity.

Additional results for four other satellites are shown in Fig. 3.13, proving the algorithm works regardless of the Galileo satellite employed.

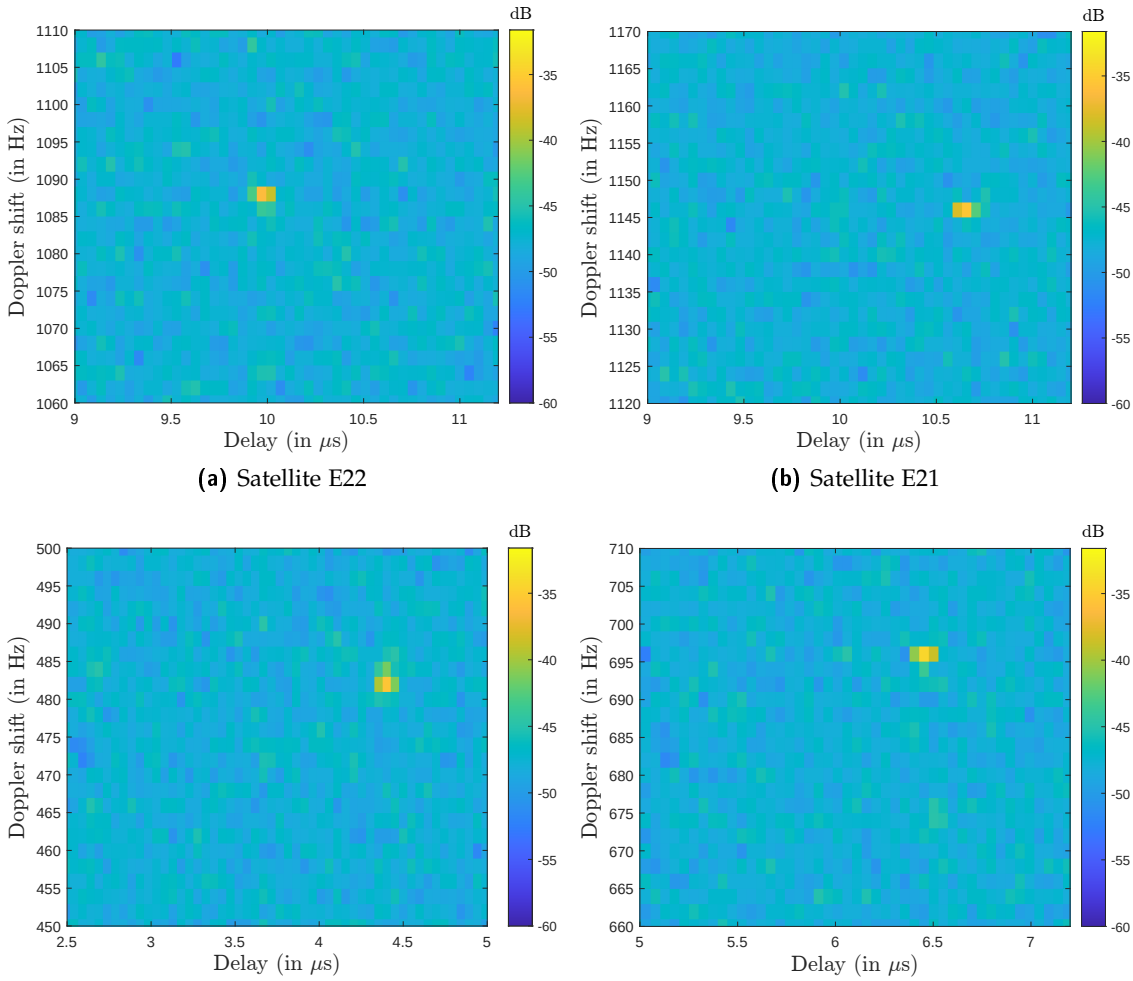

(a) Satellite E22

(b) Satellite E21

(c) Satellite E11

(d) Satellite E15

Figure 3.13.: Delay/Doppler plot, multi-frame processing, $T_{\text{int}} = 8$ s, $T_f = 0.5$ s, $\widehat{a}_{0,n} = a_{0,n}$ m/s^2, different satellites.

4. GNSS-Based Passive Multistatic Radar

In practice, the potential of the bistatic case studied in Chapter 3 is very limited due to the low transmit power of the global navigation satellite system (GNSS) satellites. In relation to this, the low maximum detection range that can be obtained in the bistatic case limits in turn the applicability of the concept. Therefore, it is of special interest to investigate the possibility of employing several simultaneous illuminator of opportunity (IoO)s to improve the signal processing gain and enhance the detection performance of the system. It is therefore of interest to first analyze the link budget performance of the multistatic case and the potential of employing several satellites in comparison with the bistatic approach. Due to the spatial separation between satellites, the reflected signals originating from the different satellites are assumed to be arriving at the ego-aircraft spatially incoherent from one another. The link budget is obtained as in the previous case for a $P_d = 0.75$ and a $P_{\text{fa}} = 10^{-4}$. The result of the analysis is depicted in Fig. 4.1.

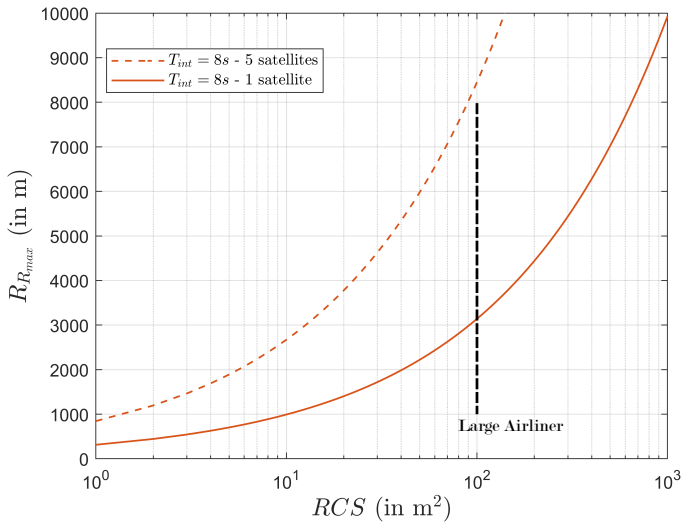

Figure 4.1.: Maximum detection range comparison.

In order to achieve a combined delay/Doppler map that integrates all the target energy present in the different bistatic links, a multistatic combination approach has to be developed. There have been some GNSS-based passive multistatic radar research works, among which two main options for the implementation of the multistatic combination algorithm stand out. On one hand, the one considered in [6] focuses on the geometrical relationship between the bistatic and target-to-receiver (Rx) ranges in order to modify the cross-ambiguity function (CAF) data and convert all delay/Doppler maps respective to the target-to-Rx range. On the other hand, in [17], the data fusion is based on space–time

integration. Due to the similarities with the target migration compensation (TMC) approach of [6], the multistatic compensation approach published therein is taken as the one to be based on. According to Fig. 2.7, the aforementioned fusion would be of the plot fusion type.

To begin with, an overview of the system is presented with the updated system block diagram depicted in Fig. 4.2. Here it can be seen that the different bistatic links are first undergoing the same multi-frame processing in Fig. 3.10, following which they undergo a transformation process. In this stage, the delay/Doppler maps associated with the different satellites are translated to a common target-to-Rx framework to allow for their combination.

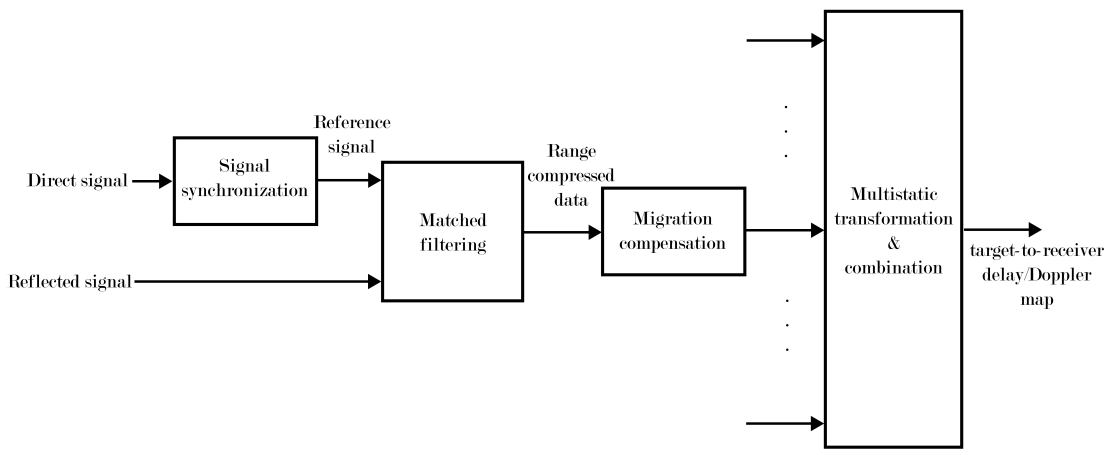

Figure 4.2.: Multistatic processing system block diagram.

4.1. Multistatic Geometry

With the objective of translating the different bistatic delay/Doppler maps to a common domain, the geometry has to be first analyzed. To allow for this, a simple scenario with three different satellites is considered. A representation of the space distribution of the system components as well as the relevant line of sight (LoS) vectors are depicted in Fig. 4.3.

In Chapter 3, the delay/Doppler maps were obtained as a result of the correlation between the direct and the reflected signals. This essentially means that the delay and Doppler are a function of the range difference between the reflected and the direct signal path and its rate of change. This range difference is denoted $R_{D_i}(t)$ and is expressed as

$$R_{D_i}(t) = \left|\overrightarrow{R_{T_i}(t)}\right| + \left|\overrightarrow{R_R(t)}\right| - \left|\overrightarrow{R_{B_i}(t)}\right| \ , \tag{4.1}$$

where $\left|\overrightarrow{R_{T_i}(t)}\right|$ is the range between the ith transmitter (Tx) and the target, $\left|\overrightarrow{R_{B_i}(t)}\right|$

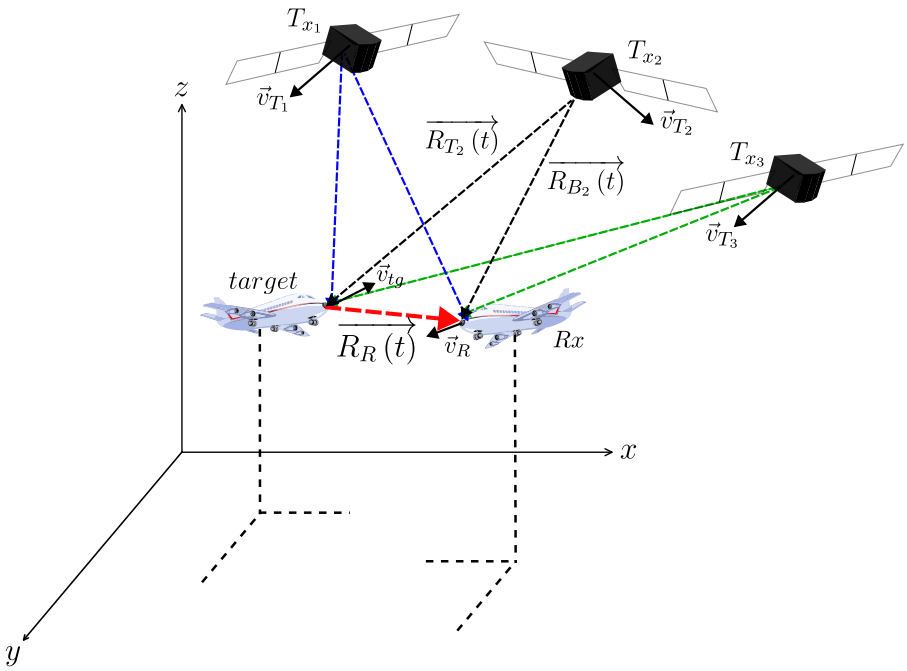

Figure 4.3.: Multistatic geometry of interest.

denotes the range between the ith Tx and the Rx, and $\left|\overrightarrow{R_R(t)}\right|$ represents the the target-to-Rx range. Due to the dependence of $R_{D_i}(t)$ on the subscript i, i.e., on the satellite used, the delay/Doppler maps associated with the different satellites are different from one another, as also shown in Fig. 3.13. As such, the different maps can not just be trivially combined, and a transformation to a domain that is common to the different bistatic links has to be performed first. From Fig. 4.3 it can be seen that the target-to-Rx distance $\left|\overrightarrow{R_R(t)}\right|$ is common to all satellites at all points in time. Accounting for this, the extracted range difference $R_{D_i}(t)$ can be expressed as a function of $\left|\overrightarrow{R_R(t)}\right|$ as:

$$\begin{aligned} R_{D_i}(t) &= \left|\overrightarrow{R_R(t)}\right| + \left(\left|\overrightarrow{R_{T_i}(t)}\right| - \left|\overrightarrow{R_{B_i}(t)}\right|\right) \\ R_{D_i}(t) &= \left|\overrightarrow{R_R(t)}\right| + \Delta R_{D_i}(t)\ , \end{aligned} \tag{4.2}$$

where $\Delta R_{D_i}(t)$ then expresses the difference between $\left|\overrightarrow{R_{T_i}(t)}\right|$ and $\left|\overrightarrow{R_{B_i}(t)}\right|$.

Since the objective is to transform the already compensated delay/Doppler maps, i.e., after the TMC stages, the transformation would only depend on the geometry at $t = 0$ s. With this in mind, the time dependency is eliminated for simplicity and the magnitude of the vectors is hereinafter denoted as $\left|\overrightarrow{R_{T_i}(t)}\right| = R_{T_i}$, $\left|\overrightarrow{R_R(t)}\right| = R_R$, and $\left|\overrightarrow{R_{B_i}(t)}\right| = R_{B_i}$. Equation (4.2) can therefore be expressed as

$$R_{D_i} = R_R + \Delta R_{D_i}\ . \tag{4.3}$$

In what follows, it is of interest to obtain an analytical expression for $\Delta R_{D_i}(t)$ such that to be able to extract it from the retrieved maps.

The following geometry analysis is based on a similar analysis carried out in [6]. The equations derived in [6] are therefore extended for the scenario studied here, since the target and Rx cannot be assumed to have the same altitude. Without a loss of generality, the Rx is placed at the origin of the coordinate system, with the coordinates of the three components being given as:

$$\begin{aligned} T_{X_i} &: (x_i, y_i, z_i) \\ target &: (x_{tg}, y_{tg}, z_{tg}) \\ R_X &: (0,0,0) \ . \end{aligned} \tag{4.4}$$

These coordinates can in turn be expressed as function of the geometry parameters as:

$$\begin{cases} x_i = R_{B_i} \cos\theta_i \cos\phi_i \\ y_i = R_{B_i} \cos\theta_i \sin\phi_i \\ z_i = R_{B_i} \sin\theta_i \ , \end{cases} \\ \begin{cases} x_{tg} = R_R \cos\theta_{tg} \cos\phi_{tg} \\ y_{tg} = R_R \cos\theta_{tg} \sin\phi_{tg} \\ z_{tg} = R_R \sin\theta_{tg} \ , \end{cases} \tag{4.5}$$

where, θ_{tg}, ϕ_{tg}, θ_i, and ϕ_i are the azimuth and elevation angles of the target and the T_{x_i}, respectively. They can also be defined as the direction of arrival (DOA) angles of the direct signal, those relative to the Tx, T_{x_i}, and the reflected signals, those relative to the target. These angles are depicted in Fig. 4.4.

From (4.2) it is known that $\Delta R_{D_i} = \left|\overrightarrow{R_{T_i}}\right| - \left|\overrightarrow{R_{B_i}}\right|$, however, the Tx-to-target LoS vector, $\overrightarrow{R_{T_i}}$, is dependent on the target coordinates, which are unknown in practice. As a result, an expression for this geometry dependent component is searched for. Since $R_{B_i}, R_{T_i} >> R_R \quad , \forall i$, the angle $\angle R_{B_i} R_{T_i}$, i.e., the angle between these two vectors can be considered to be very small in practice. With this in mind, the difference between the two vectors can be approximated as the difference between one vector and the projection of the second onto this vector. This is expressed as

$$\Delta R_{D_i} = \left|\overrightarrow{R_{T_i}}\right| - \left|\overrightarrow{R_{B_i}}\right| \approx \overrightarrow{R_{T_i}} \frac{\overrightarrow{R_{B_i}}}{\left|\overrightarrow{R_{B_i}}\right|} - \left|\overrightarrow{R_{B_i}}\right| \ . \tag{4.6}$$

Inserting the coordinates of (4.4) into (4.6), the following is obtained:

$$\begin{aligned} \Delta R_{D_i} &\approx \frac{x_i^2 + y_i^2 + z_i^2 - (x_{tg} \times x_i + y_{tg} \times y_i + z_{tg} \times z_i)}{\sqrt{x_i^2 + y_i^2 + z_i^2}} - \sqrt{x_i^2 + y_i^2 + z_i^2} \\ &= \frac{x_i^2 + y_i^2 + z_i^2 - (x_{tg} \times x_i + y_{tg} \times y_i + z_{tg} \times z_i) - (x_i^2 + y_i^2 + z_i^2)}{\sqrt{x_i^2 + y_i^2 + z_i^2}} \\ \Delta R_{D_i} &= -\frac{x_{tg} \times x_i + y_{tg} \times y_i + z_{tg} \times z_i}{\sqrt{x_i^2 + y_i^2 + z_i^2}} \ . \end{aligned} \tag{4.7}$$

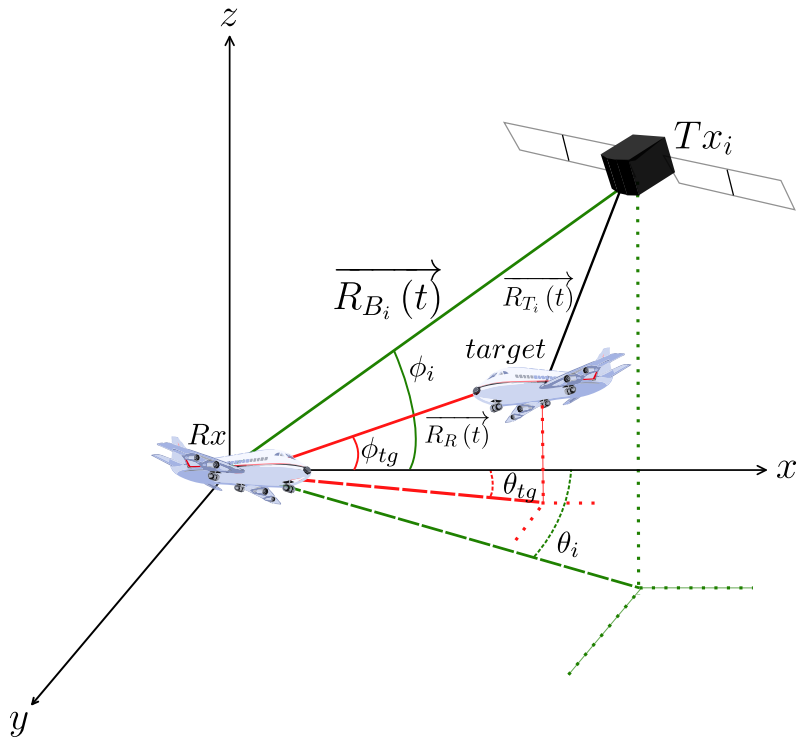

Figure 4.4.: Multistatic geometry transformation.

Next, substituting (4.5) into (4.7), the equality results

$$\Delta R_{D_i} = -\frac{R_R R_{B_i}\left[\cos(\theta_i)\cos(\phi_i)\cos(\theta_{tg})\cos(\phi_{tg}) + \cos(\theta_i)\sin(\phi_i)\cos(\theta_{tg})\sin(\phi_{tg})\right]}{\sqrt{R_{B_m}^2\left[\cos(\theta_i)^2\cos(\phi_i)^2 + \cos(\theta_i)^2\sin(\phi_i)^2 + \sin(\theta_i)^2\right]}}$$

$$-\frac{R_R R_{B_i}\left[\sin(\theta_i)\sin(\theta_{tg})\right]}{\sqrt{R_{B_m}^2\left[\cos(\theta_i)^2\cos(\phi_i)^2 + \cos(\theta_i)^2\sin(\phi_i)^2 + \sin(\theta_i)^2\right]}}$$

$$\Delta R_{D_i} = -R_R\left[\cos(\theta_i)\cos(\theta_{tg})\cos(\phi_i - \phi_{tg}) + \sin(\theta_i)\sin(\theta_{tg})\right] \ . \tag{4.8}$$

Having obtained a geometry-dependant closed-up expression for ΔR_{D_i}, (4.3) can be expressed as

$$\begin{aligned} R_{D_i} &\approx R_R \times \left[1 - \left(\cos(\theta_i)\cos(\theta_{tg})\cos(\phi_i - \phi_{tg}) + \sin(\theta_i)\sin(\theta_{tg})\right)\right] \\ &= R_R \times \xi_i\left(\phi_{tg}, \theta_{tg}, \phi_i, \theta_i\right) \ , \end{aligned} \tag{4.9}$$

which equally applies to the relation between both delays as

$$\tau_{D_i} \approx \tau_R \times \xi_i\left(\phi_{tg}, \theta_{tg}, \phi_i, \theta_i\right) \ . \tag{4.10}$$

The transformation of the Doppler axis can then be obtained as

$$\begin{aligned}\nu_{D_i} &= -\frac{1}{\lambda}\frac{\partial R_{D_i}}{\partial t} \approx -\frac{1}{\lambda}\frac{\partial}{\partial t}\left(R_R \times \xi_i\left(\phi_{tg},\theta_{tg},\phi_i,\theta_i\right)\right)\\ \nu_{D_i} &\approx -\frac{1}{\lambda}R_R\xi_i\left(\phi_{tg},\theta_{tg},\phi_i,\theta_i\right) - \frac{1}{\lambda}R_R\dot{\xi}_i\left(\phi_{tg},\theta_{tg},\dot{\phi_{tg}},\dot{\theta_{tg}},\phi_i,\theta_i,\dot{\phi}_i,\dot{\theta}_i\right)\ ,\end{aligned} \tag{4.11}$$

resulting the approximation of interest

$$\nu_{D_i} \approx \nu_R\xi_i\left(\phi_{tg},\theta_{tg},\phi_i,\theta_i\right) - \frac{R_R}{\lambda}\dot{\xi}_i\left(\phi_{tg},\theta_{tg},\dot{\phi_{tg}},\dot{\theta_{tg}},\phi_i,\theta_i,\dot{\phi}_i,\dot{\theta}_i\right)\ . \tag{4.12}$$

In (4.12), a dependency on the derivative of ξ_i denoted here as $\dot{\xi}_i$ can be seen. An expression for this derivative is obtained next. For this the term ξ_i is first divided into two components as follows

$$\begin{aligned}\xi_i\left(\phi_{tg},\theta_{tg},\phi_i,\theta_i\right) &= [1-(\cos(\theta_i)\cos(\theta_{tg})\cos(\phi_i-\phi_{tg})+\sin(\theta_i)\sin(\theta_{tg}))]\\ \xi_i\left(\phi_{tg},\theta_{tg},\phi_i,\theta_i\right) &= [1-(a+b)]\ ,\end{aligned} \tag{4.13}$$

where a is given as

$$a = \cos(\theta_i)\cos(\theta_{tg})\cos(\phi_i-\phi_{tg})\ , \tag{4.14}$$

and b takes the form

$$b = \sin(\theta_i)\sin(\theta_{tg})\ . \tag{4.15}$$

Consequently, the derivative of ξ_i is obtained as

$$\frac{\partial\xi_i\left(\phi_{tg},\theta_{tg},\phi_i,\theta_i\right)}{\partial t} = -\left(\frac{\partial a}{\partial t}+\frac{\partial b}{\partial t}\right)\ . \tag{4.16}$$

Firstly, the derivative of a is computed as

$$\begin{aligned}\frac{\partial a}{\partial t} &= (\cos(\theta_i))'\cos(\theta_{tg})\cos(\phi_i-\phi_{tg}) + \cos(\theta_i)\left(\cos(\theta_{tg})\right)'\cos(\phi_i-\phi_{tg})\\ &\quad + \cos(\theta_i)\cos(\theta_{tg})\left(\cos(\phi_i-\phi_{tg})\right)'\\ \frac{\partial a}{\partial t} &= \left(-\sin(\theta_i)\dot{\theta}_i\right)\cos(\theta_{tg})\cos(\phi_i-\phi_{tg}) + \cos(\theta_i)\left(-\sin(\theta_{tg})\dot{\theta}_{tg}\right)\cos(\phi_i-\phi_{tg}) +\\ &\quad \cos(\theta_i)\cos\theta_{tg}\left(-\sin(\phi_i-\phi_{tg})\left(\dot{\phi}_i-\dot{\phi}_{tg}\right)\right)\ .\end{aligned} \tag{4.17}$$

Secondly, the derivative of b follows

$$\frac{\partial b}{\partial t} = (\sin(\theta_i))'\sin(\theta_{tg}) + \sin(\theta_i)\left(\sin(\theta_{tg})\right)' = \cos(\theta_i)\sin(\theta_{tg})\dot{\theta}_i + \sin(\theta_i)\cos(\theta_{tg})\dot{\theta}_{tg}\ . \tag{4.18}$$

Lastly, both (4.17) and (4.18) results are inserted in (4.16), resulting

$$\begin{aligned}
&\frac{\partial \xi_i(\phi_{tg}, \theta_{tg}, \phi_i, \theta_i)}{\partial t} = \dot{\xi}_i(\phi_{tg}, \theta_{tg}, \dot{\phi_{tg}}, \dot{\theta_{tg}}, \phi_i, \theta_i, \dot{\phi}_i, \dot{\theta}_i) = -\left(\frac{\partial a}{\partial t} + \frac{\partial b}{\partial t}\right) \\
&= -\Big[\sin(\theta_i)\left(\cos(\theta_{tg})\,\dot{\theta}_{tg} - \cos(\theta_{tg})\,\dot{\theta}_i \cos(\phi_i - \phi_{tg})\right) + \cos(\theta_i)\left(\sin(\theta_{tg})\,\dot{\theta}_i\right. \\
&\quad - \sin(\theta_{tg})\,\dot{\theta}_{tg}\cos(\phi_i - \phi_{tg}) - \sin(\phi_i - \phi_{tg})(\dot{\phi}_i - \dot{\phi}_{tg})\cos(\theta_{tg})\Big)\cos(\theta_i)\left(\sin(\theta_{tg})\right. \\
&\quad \left.(\dot{\theta}_i - \dot{\theta}_{tg}\cos(\phi_i - \phi_{tg})) - \sin(\phi_i - \phi_{tg})(\dot{\phi}_i - \dot{\phi}_{tg})\cos(\theta_{tg})\right) \\
&\quad + \sin(\theta_i)\cos(\theta_{tg})\left(\dot{\theta}_{tg} - \dot{\theta}_i\cos(\phi_i - \phi_{tg})\right)\Big] .
\end{aligned} \tag{4.19}$$

The transformation to be applied then in delay results

$$\tau_R \approx \frac{\tau_{D_i}}{\xi_i\left(\phi_{tg}, \theta_{tg}, \phi_i, \theta_i\right)} , \tag{4.20}$$

while the one in Doppler is

$$\nu_R \approx \frac{\nu_{D_i} + \frac{R_R}{\lambda}\dot{\xi}_i\left(\phi_{tg}, \theta_{tg}, \dot{\phi_{tg}}, \dot{\theta_{tg}}, \phi_i, \theta_i, \dot{\phi}_i, \dot{\theta}_i\right)}{\xi_i\left(\phi_{tg}, \theta_{tg}, \phi_i, \theta_i\right)} . \tag{4.21}$$

The necessary transformation operations are therefore: 1) a delay and Doppler division by the factor ξ_i, hereinafter referred to as rescaling operations, and 2) a displacement component in the Doppler domain in the form of a subtraction. With the above developed equations, a transformation between the domains of interest can be carried out. The approach used to achieve this is described in the following section.

4.2. Implemented Approach

The focus of this section is put on the implementation of the transformations defined by (4.20) and (4.21), respectively. Due to the other similarities shared with the work in [6], an approach similar to the one proposed in [6] is followed. The rescaling operations are therefore implemented by means of a chirp-Z transform (CZT) each, while the displacement is compensated by a phase term, similar to the migration compensation in Chapter 3.

To begin with, the rescaling in delay and Doppler is essentially a resampling of the data at a new rate of interest. The CZT has been previously used in synthetic aperture radar (SAR) applications for range and azimuth rescaling [41]. By modifying the angular spacing of the samples, the data of interest can be modified to fit the new desired rescaling. In particular for the envisioned application, the angular spacing factor is set to be equal to the rescaling factor [6]. Moreover, the rescaling factor is an estimate of the parameter ξ_i, denoted by $\widehat{\xi}_i$. As described in [6], when the parameter ξ_i is such that $\xi_i > 1$, a compression of the delay and Doppler axis is obtained. Consequently, doing this would compress the available power within the new axis limits, inherently

increasing the overall mean power of the delay/Doppler map. However, since the peak power of the signal in the individual delay/Doppler maps is not increased as a result of the transformation, only the noise is enhanced, with the signal-to-noise ratio (SNR) of the transformed maps reduced to an extent dependent on the value of ξ_i. The opposite effect is being expected for the case when $\xi_i < 1$, where the dilation of the axis would intuitively lead to a spread of the power.

Unlike the two rescaling operations, the displacement in Doppler $-R_R/\lambda\dot{\xi}_i$ is compensated by multiplying the data by a phase term given as $e^{j2\pi t' c_0/\lambda\hat{\dot{\xi}}_i m T_r}$.

The above described processing is accounted for in Fig. 4.5, which can be seen as an extension of Fig. 3.10 including the transformation and combination.

As already mentioned in Section 3.4.2, the estimates $\hat{\xi}_i$ and $\hat{\dot{\xi}}_i$ of the geometry dependent parameters are assumed to be known. This allows to test the performance of the algorithm while avoiding the impact of other performance limitations. It is important to note that the study and implementation of an approach for reliably obtaining this estimates is outside of the scope of this work.

Results and Analysis

Now, the updated signal processing chain in Fig. 4.5 is tested on the simulated signals from the Galileo satellites E02, E22, E11, and E21. If the transformation is successful, all the target-to-Rx maps should present their most powerful delay/Doppler cell in that relative to the the target-to-Rx distance, being thus able to combine these results in the subsequent step. For the scenario at hand, the target-to-Rx distance and its rate leads to a delay $\tau_0 = 5.43$ µs and a Doppler $\nu_0 = 582$ Hz. The delay/Doppler cell closest to these values will then be the ones expected to have the highest peak power in all the target-to-Rx delay/Doppler maps.

In order to assess purely the performance of the transformation, the analysis is initially done for a noise-free scenario. The results obtained for satellite E02, E22, E11, and E21 are depicted in: a) Fig. 4.6, b) Fig. 4.7, c) Fig. 4.8, and d) Fig. 4.9, respectively. Each of the results is shown together with the original multi-frame noise-free result, i.e., in Fig 4.6a, Fig 4.7a, Fig 4.8a, and Fig 4.9a with the objective of displaying the result before and after the transformation. An overview of the value of ξ_i for these four satellites can be seen in Table 4.1.

Table 4.1.: ξ_i overview.

Satellite	ξ_i
E02	1.0451
E22	1.8336
E11	0.8120
E21	1.9552

The parameter associated with satellite E02 in Fig. 4.6b is then $\xi_{E02} = 1.0451$. Since this value is very close to 1, only a minor rescaling is needed when starting from the

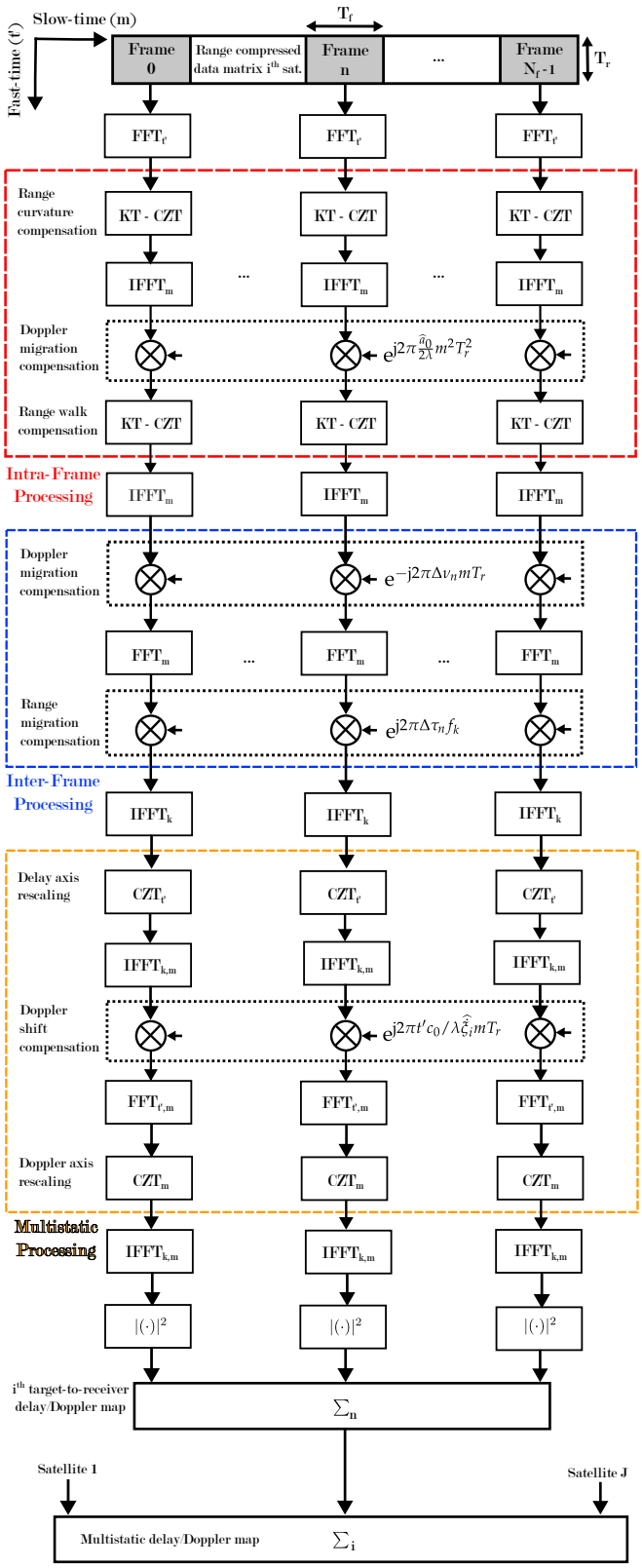

Figure 4.5.: Multistatic multi-frame processing.

bistatic result depicted in Fig. 4.6a. This is understandable since the original result retrieved by the bistatic processing is very similar to the target-to-Rx one.

In contrast to satellite E02 case, the second case analyzed, i.e., the satellite E22, is associated with $\xi_{E22} = 1.8336$. As such, the underlying transformation needed is more extensive than in the case before, which can be confirmed when analyzing the results in Fig. 4.7a, where the maximum power delay/Doppler cell lies far away from the target-to-Rx one depicted in Fig. 4.7b. It is important to note here that the axes limits are different in each plot.

Big differences between the bistatic and the target-to-Rx maps are associated with geometries where the angle $\angle R_{B_i} R_{T_i}$ is almost 0°, assuming a fixed realistic R_R. In this case, the ranges R_{T_i}, R_{B_i} are noticeably different, which directly relates to a higher value of ΔR_{D_i}, as it is expressed in (4.8). This, in turn, triggers notable differences between R_{D_i} and R_R, clearly motivated by (4.3). Consequently, the bistatic and the target-to-Rx maps present big differences that require a more extensive transformation. The selection of satellites with a low elevation are more prone to give rise to these geometries, as for most orbit paths the angle $\angle R_{B_i} R_{T_i}$ is closer to 0 in the low elevation part of the path. The ephemeris data confirms this is the case for the studied satellites, as the elevation of the satellite E02 is $\phi_{E02} = 71.4°$ while that of satellite E22 is $\phi_{E22} = 10.7°$ during the simulation.

Next, the attention is turned to the geometry associated with satellite E11 which is associated with $\xi_i < 1$ and gives rise to the transformation depicted in Fig. 4.8.

In Fig. 4.8b the successful transformation performed for satellite E11 can be seen. It is worth noting here that the bistatic result shown in 4.8a shows a lower retrieved delay and Doppler values than the final target-to-Rx in Fig. 4.8b. This is indeed related to the parameter being $\xi_i < 1$, more specifically its value is $\xi_{E11} = 0.8120$.

Lastly, a fourth transformation for satellite E21, with $\xi_{E21} = 1.9552$, is depicted in Fig. 4.9b, with an underlying geometry similar to the one of satellite E22.

As it can be seen, the transformation is successful for all tested satellites, translating the target delay/Doppler cell from the bistatic map to the delay/Doppler cell of interest in the new reference map. In addition, it can be seen that in the noise-free case there is no impact yet of the different extents of the different transformations. These individual maps can now be combined to get the overall multistatic target-to-Rx map. This essentially combines all the available energy in the delay/Doppler cell of interest such that to increase the target signal power within this cell and improve its detection capabilities. The multistatic combined map is shown in Fig. 4.10 in the noise-free case.

A comparison of the peak powers obtained in the individual target-to-Rx maps as well as in the multistatic map is shown in Table 4.2. Here, it can be seen that when combining the four bistatic maps, a target signal power gain of 5.92 dB is achieved in relation to the average target signal power retrieved in the individual delay/Doppler maps. It can be therefore noted that the combination is performed successfully and it is able to enhance the retrieved target power, which is key to the goal of this work. However the final objective of the transformation is to increase the signal processing

gain, which is related to the overall output SNR after the multistatic combination. For this, the presence of noise has to be taken into account.

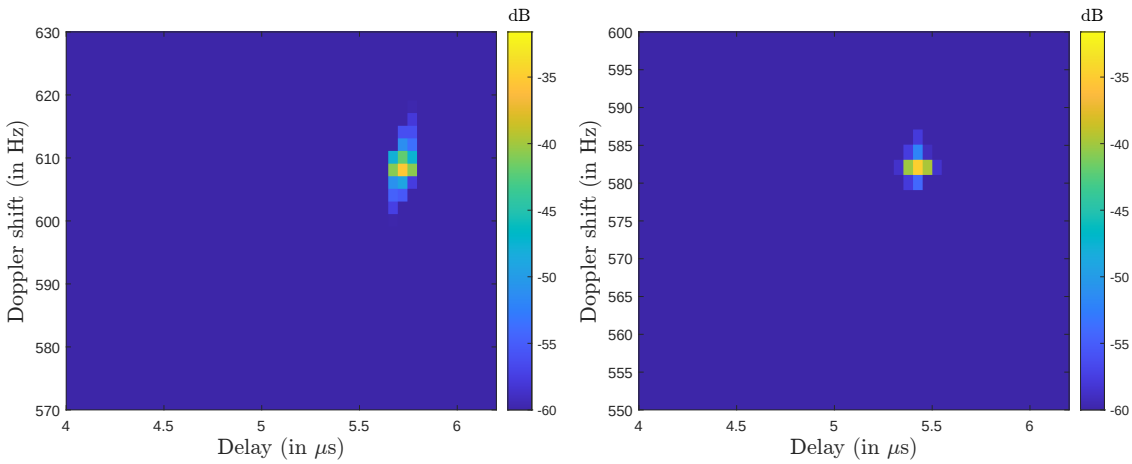

(a) Bistatic map **(b)** Target-to-Rx map

Figure 4.6.: Domain transformation, noise-free, compensated, $T_{\text{int}} = 8$ s, sat. E02.

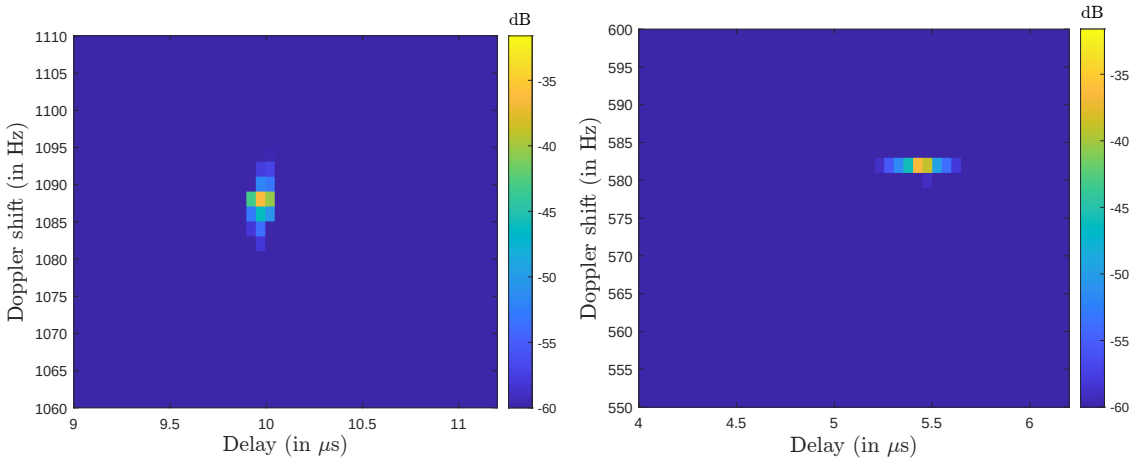

(a) Bistatic map **(b)** Target-to-Rx map

Figure 4.7.: Domain transformation, noise-free, compensated, $T_{\text{int}} = 8$ s, sat. E22.

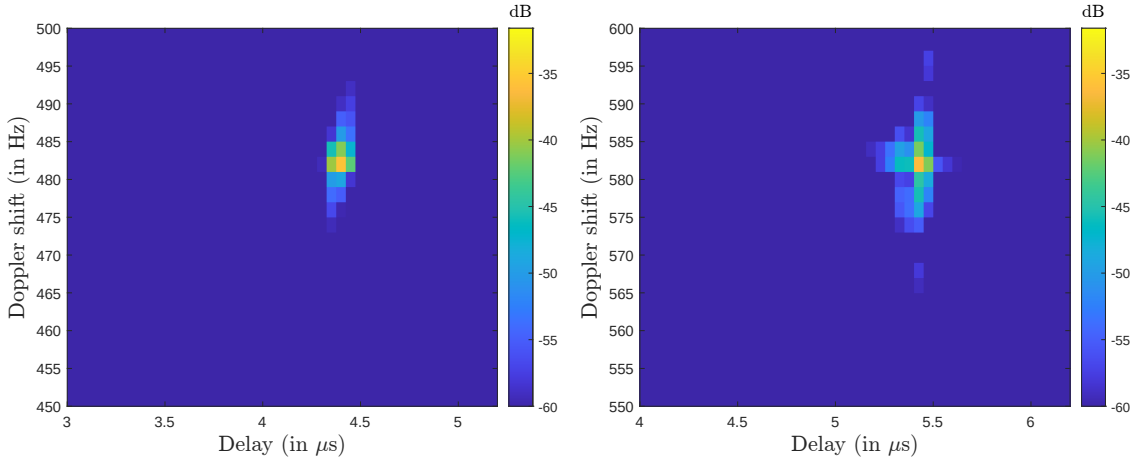

(a) Bistatic map **(b)** Target-to-Rx map

Figure 4.8.: Domain transformation, noise-free, compensated, $T_{\text{int}} = 8$ s, sat. E11.

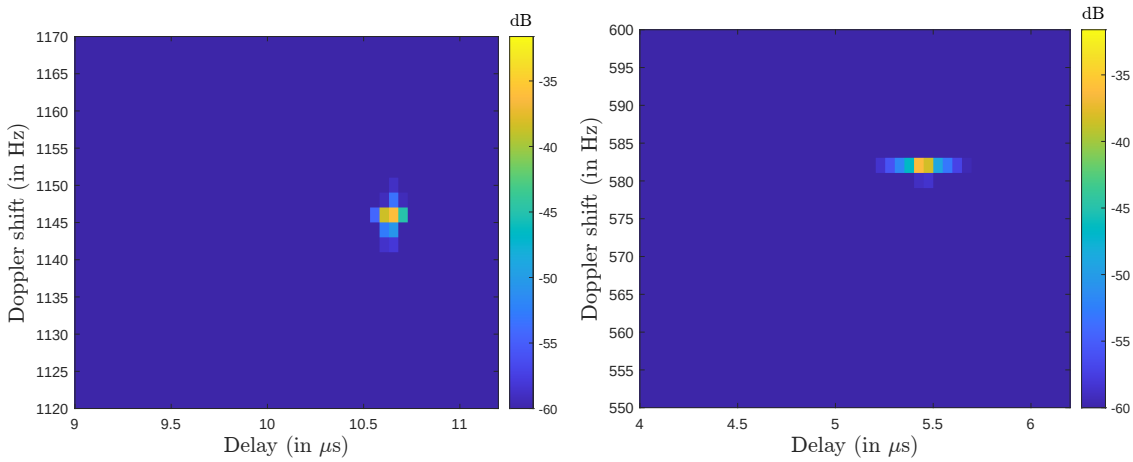

(a) Bistatic map **(b)** Target-to-Rx map

Figure 4.9.: Domain transformation, noise-free, compensated, $T_{\text{int}} = 8$ s, sat. E21.

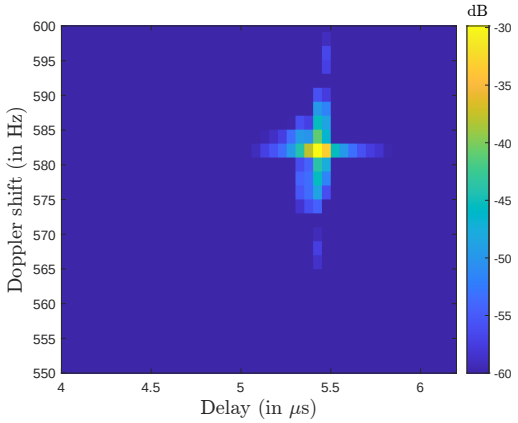

Figure 4.10.: Multistatic delay/-Doppler map, noise-free, compensated, $T_{\text{int}} = 8$ s, sat. E02 + sat. E22 + sat. E11 + sat. E21.

Table 4.2.: Multistatic map peak power.

Satellite	Peak power (in dB)
E02	-34.83
E22	-36.53
E11	-36.2
E21	-36.18
Multistatic map	-29.96

The last step is therefore to test the performance of the algorithm in the presence of noise. The results obtained for satellite E02, E22, E11, and E21 are depicted in: a) Fig. 4.11, b) Fig. 4.12, c) Fig. 4.13, and d) Fig. 4.14, respectively. Similar to the noise-free case, the maps obtained after the transformation are shown along the bistatic ones. The characteristics of the noise are again the ones detailed in Table 3.2.

Given that for satellite E02 the rescaling parameter is $\xi_{E02} = 1.0541$, the minimal rescaling and associated compression of the axes gives rise to only a minimal noise enhancement as a result of the transformation. As such, the output SNR remains almost unchanged after the transformation and this result can be used for performing the subsequent multistatic combination.

In contrast to E02, satellite E22 is associated with $\xi_{E22} = 1.8336$. The higher value of this parameter induces a compression of the power which leads to a noise enhancement, as it can be clearly seen in Fig. 4.12b. As stated previously, this effect is foreseen for the cases where ξ_i is not close to 1. Nevertheless, the extent of this effect was unknown for the scenario of interest and is part of the findings of this work. As such, the delay/Doppler map in Fig. 4.12b presents a much lower SNR than the bistatic case in Fig. 4.12a. This makes it unsuitable for the combination stage as it would result in a loss of the overall SNR, which is other key against what is needed.

Furthermore, an unforeseen phenomena was encountered while testing different geometry configurations. In particular, for cases where the rescaling parameter $\xi_i < 1$, the redistribution of the available power as a result of the rescaling is not done uniformly. This is the case of satellite E11 presented in Fig. 4.13. As it can be seen, for this particular geometry, the retrieved maximum power delay/Doppler cell in Fig. 4.13a has a lower delay and Doppler value than the one of interest in the reference map. The rescaling parameter $\xi_{E11} = 0.8120$ would therefore result in a spread of the available power. Intuitively, this was expected to lower the noise, the opposite effect of that depicted for

cases with $\xi_i > 1$. However, the actual results show complicated artifacts in the delay axis, along with an unexpected noise enhancement. This effect was not addressed in any other research works and has to be therefore thoroughly understood before devising ways to mitigate it. The analysis of the origin of these artifacts lies outside of the scope of this work and will be addressed in the planned future work.

Lastly, the result for satellite E21 is similar with the one for satellite E22 due to their similar ξ_i value. The transformed delay/Doppler map for this satellite is shown in Fig 4.14b.

The multistatic result that combines the four target-to-Rx is shown in Fig. 4.15. There, it can be clearly seen that the combination does not improve the output SNR in comparison to the individual bistatic delay/Doppler maps. As a result of both the high noise enhancement when ξ_i is not close to one and the artifacts when $\xi_i < 1$, the target-to-Rx results with noise should not be directly combined as a lower output SNR is retrieved in comparison to the individual bistatic maps. Additional results for each case are included in Appendix B, where it can be seen that each of the results are replicable and consistent with the initial understanding of the artifacts. Bearing in mind that the transformation of the delay/Doppler cell of interest is performed successfully, the goals foreseen for this work have been achieved.

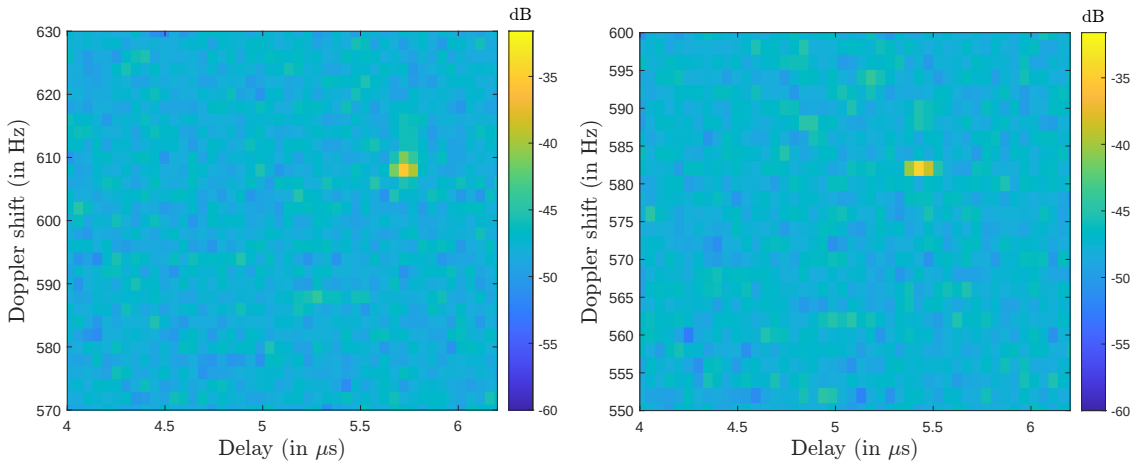

(a) Bistatic map **(b)** Target-to-Rx map

Figure 4.11.: Domain transformation, compensated, $T_{\text{int}} = 8$ s, sat. E02.

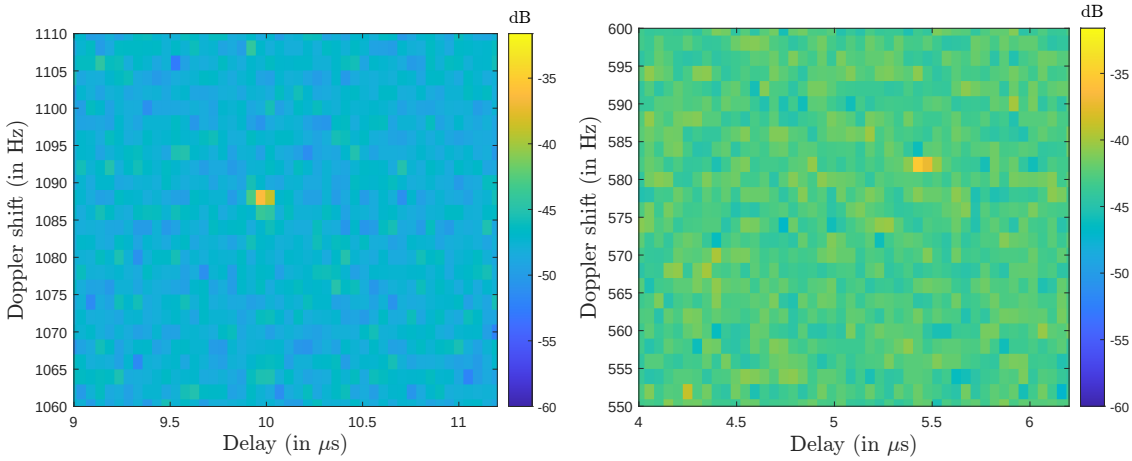

(a) Bistatic map **(b)** Target-to-Rx map

Figure 4.12.: Domain transformation, compensated, $T_{\text{int}} = 8$ s, sat. E22.

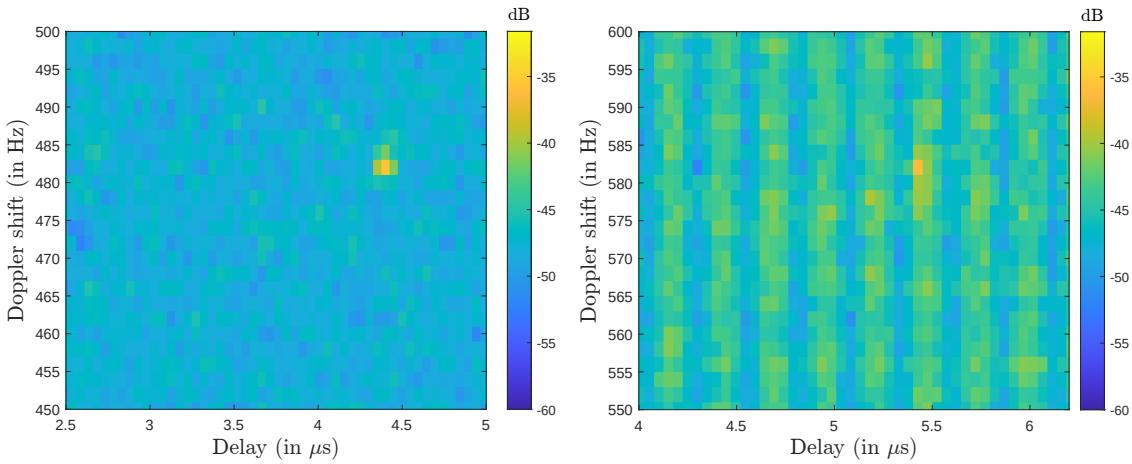

(a) Bistatic map **(b)** Target-to-Rx map

Figure 4.13.: Domain transformation, compensated, $T_{\text{int}} = 8$ s, sat. E11.

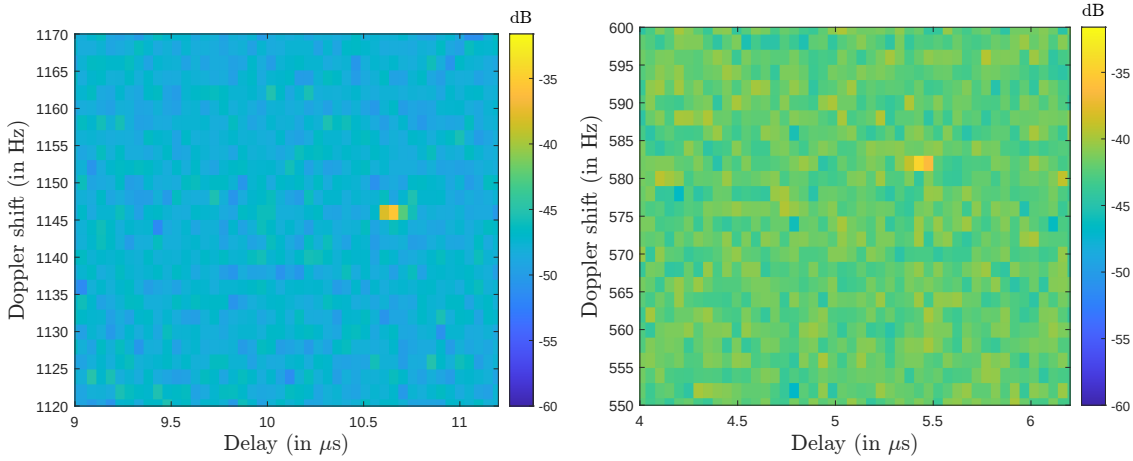

(a) Bistatic map **(b)** Target-to-Rx map

Figure 4.14.: Domain transformation, compensated, $T_{\text{int}} = 8$ s, sat. E21.

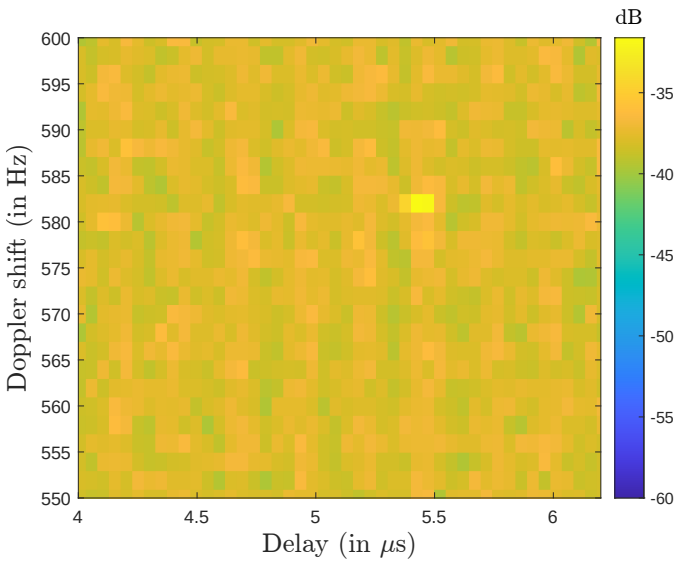

Figure 4.15.: Multistatic delay/Doppler map, compensated, $T_{\text{int}} = 8$ s, sat. E02 + sat. E22 + sat. E11 + sat. E21.

5. Conclusion and Future Work

In this work, the idea of employing the global navigation satellite system (GNSS) satellites as illuminators of opportunity has been investigated for passive detection purposes in an air-to-air (A2A) scenario. The motivation for this work is the need for a non-cooperative A2A situational awareness application. The aim is therefore to explore the possibility of employing the signal from several GNSS satellites in a passive multistatic radar scheme. The main contributions and findings of this work can be derived from Chapter 3 and Chapter 4 and are summarized next.

From the results presented in Chapter 3, several conclusions can be drawn. Firstly, the link budget analysis of the scenario at hand demonstrated the need for a long integration time. To this end, the implications that the use of a long integration time have on the detection performance and target energy migration were assessed for the passive bistatic case. The analysis confirmed the need for target migration compensation (TMC) techniques in order to allow for the aircraft detection. Accordingly, the performance of state-of-the-art TMC algorithms was evaluated for the scenario of interest. As a result, the presence of jerk-induced migration effects was established, which have to be taken into account for the TMC. The main outcome of this analysis is the fact that the fast changing bistatic geometry makes these algorithms largely unsuitable in this case. As such, the state-of-the-art single frame and multi-frame approaches were successfully adapted and combined to account for the jerk-induced migration, and the derived hybrid processing implemented and tested. The results of this assessment have shown that the developed approach is better tailored to the scenario at hand.

Moving on to Chapter 4, multiple findings stand out. In the passive bistatic radar results it could be seen that the target energy was placed at a different delay/Doppler cell for each of the satellites. From this, the need for a multistatic transformation before the combination of the results was clear. In this respect, a state-of-the-art method was extended to match the scenario of interest and implemented. Furthermore, the underlying expressions that characterize the transformation were derived analytically. Then, a signal processing chain was developed to apply the transformations to the bistatic delay/Doppler maps. The performance of this transformation was tested first with noise-free simulations, where it could be seen that the transformation was successful and a processing gain was achieved when combining several bistatic delay/Doppler maps. Consequently, the multistatic transformation needed to enable GNSS-based multistatic radar detection was successfully achieved in the noise-free case. However, when testing the entire framework in the presence of noise, several artifacts in the form of noise enhancement could be seen for certain geometries. A thorough understanding of the origin of these artifacts is still needed since the probability that these cases appear

in reality is relatively high.

Accounting for all these aspects, a number of future research work directions can be defined.

First and foremost, it is imperative to further investigate and understand the origin of the artifacts induced by the multistatic transformation in the case with noise. A good understanding of these effects is needed in order to allow for their mitigation. The overcoming of these effects plays a key role for the feasibility of this approach in practice. Additionally, alternative multistatic combination approaches should be investigated and their performance assessed.

Equally important to mention here are the future efforts needed to investigate how to efficiently estimate the acceleration and geometry parameters estimates, since they were assumed to be known for this work. The potential leverage of machine learning technologies for this task is in particular to be assessed.

Moreover, extending the approach to encompass other GNSS constellations and frequency bands is another critical avenue for future work. With the ever-growing diversity in satellite systems and frequency bands, it is essential to adapt and validate multistatic transformation techniques across these different platforms. This will bring a higher processing gain, allowing for larger detection ranges.

Lastly, the study of multi-target scenarios should be pursued. The challenges posed by tracking and localizing multiple targets simultaneously are multifaceted and bring yet another layer of complexity, requiring additional innovative solutions. Future research can focus on developing algorithms that can handle multi-target environments efficiently, opening up new possibilities for applications in surveillance.

A. GNSS comparison

A summary of the most important characteristics has been put together and is presented in Table A.1. The information shown in the table has been gathered from [25], [27], [42]–[46]. The minimum power is defined as the minimum power received by an omnidirectional antenna on the Earth's surface. The following acronyms appear in the table: bandwidth (BW), code division multiple access (CDMA), frequency division multiple access (FDMA), Precision (P), and Coarse/Acquisition (C/A). As the outcome of this assessment, the E5 Galileo signal, with the E5a and E5b subbands, was selected as the most promising signal of opportunity for the intended application.

GNSS	GPS			GLONASS		Galileo			
Band	L1	L2	L5	G1	G2	E1	E6	E5a	E5b
Center carrier frequency (in MHz)	1575.42	1227.6	1176.45	1602.563 - 1615.5	1246 - 1257	1575.42	1278.75	1176.45	1207.14
Signal BW (in MHz)	C/A : 1.023 P : 10.23 L1C : 1.023	P : 10.23 L2C : 10.23	10.23	C/A : 0.511 P : 5.11	P : 5.11	C_{E1-B} : 1.023 C_{E1-C} : 1.023	C_{E6-B} : 5.11 C_{E6-C} : 5.11	C_{E5a-I} : 10.23 C_{E5a-Q} : 10.23	C_{E5b-I} : 10.23 C_{E5b-Q} : 10.23
Access Technique	CDMA	CDMA	CDMA	FDMA	FDMA	CDMA	CDMA	CDMA	CDMA
Chip rate (in M/s)	C/A : 1.023 P : 10.23 L1C : 1.023	P : 10.23 L2C : 10.23	10.23	C/A : 0.511 P : 5.11	P : 5.11	C_{E1-B} : 1.023 C_{E1-C} : 1.023	C_{E6-B} : 5.11 C_{E6-C} : 5.11	C_{E5a-I} : 10.23 C_{E5a-Q} : 10.23	C_{E5b-I} : 10.23 C_{E5b-Q} : 10.23
Navigation data	Yes	Yes	I : Yes Q : No	Yes	Yes	Yes	Yes	I : Yes Q : No	I : Yes Q : No
Minimum power (in dBw)	P : -161.5 C/A or L1C: -158.5	P : -164.5 L2C : -164.5	-157.9	P : N/A C/A : -161	P : N/A C/A : -167	I : -160 Q : -160	I : -158 Q : -158	I : -158 Q : -158	I : -158 Q : -158

Table A.1.: Parameter comparison of the different GNSS signals.

B. Additional Results

$\xi_i = 1.1893$

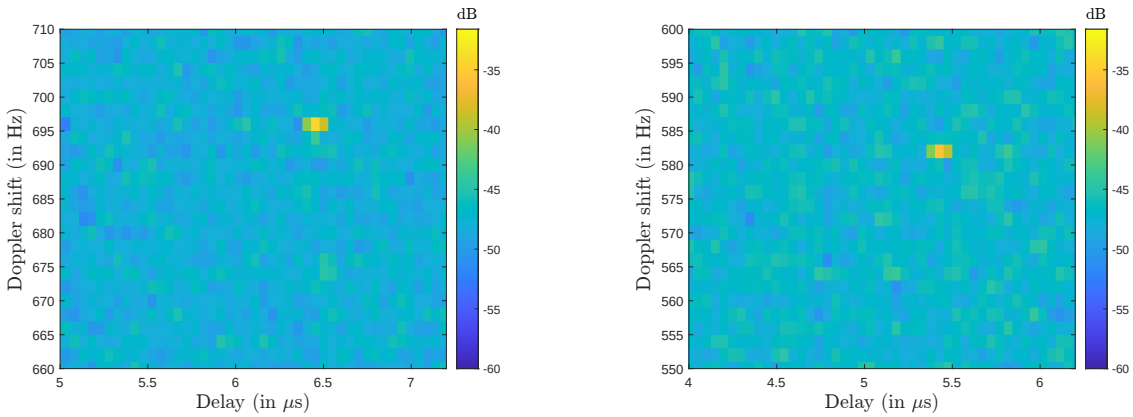

(a) Bistatic map **(b)** Target-to-receiver (Rx) map

Figure B.1.: Domain transformation, compensated, $T_{\text{int}} = 8$ s, sat. E15.

$\xi_i = 0.9276$

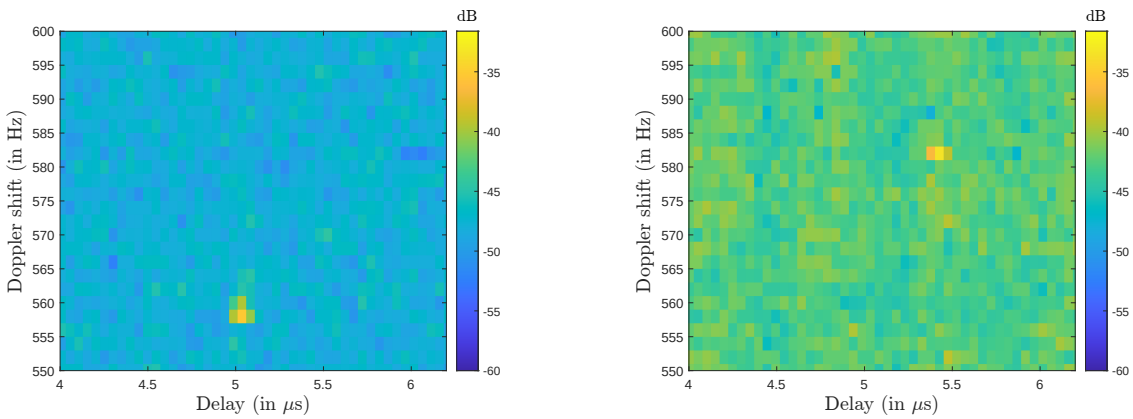

(a) Bistatic map **(b)** Target-to-Rx map

Figure B.2.: Domain transformation, compensated, $T_{\text{int}} = 8$ s, sat. E13.

List of Figures

1.1. Global air passengers per year forecast (adapted from [2]). 1
1.2. State-of-the-art situational awareness in civil air traffic. 2
1.3. GNSS-based non-cooperative situational awareness. 3

2.1. GNSS frequency bands [25]. 7
2.2. power spectral density (PSD) of the Galileo E5 signal [25]. 8
2.3. Tiered code generation (adapted from[27]). 8
2.4. Tiered code structure [27]. 9
2.5. Radar types. 11
2.6. Bistatic geometry. 12
2.7. Multistatic radar types (adapted from [29]). 14
2.8. ambiguity function (AF) of the Galileo E5a signal. 15
2.9. Dual domains (adapted from [7]). 16

3.1. Bistatic system block diagram. 17
3.2. Batches algorithm signal segmentation (adapted from [7]). 19
3.3. Max detection range vs. radar cross section (RCS) for 1 satellite and 2 different integration times. 22
3.4. Delay/Doppler plot, single frame processing, uncompensated, $T_{\text{int}} = 8$ s. 22
3.5. Single frame migration compensation processing approach. 25
3.6. Doppler shift and relative acceleration for the simulated geometry. 26
3.7. Delay/Doppler plots, single frame processing, compensated, $T_{\text{int}} = 8$ s. . 26
3.8. Delay/Doppler plot, multi-frame processing, noise-free, uncompensated, $T_{\text{int}} = 8$ s, $T_f = 0.5$ s, sat. E02. 29
3.9. Delay/Doppler plot, multi-frame processing, noise-free, intra-frame migration compensation only, $T_{\text{int}} = 8$ s, $T_f = 0.5$ s, sat. E02. 29
3.10. Multi-frame migration compensation processing approach. 31
3.11. Delay/Doppler plots, multi-frame processing, $T_{\text{int}} = 8$ s, $T_f = 0.5$ s, $\widehat{a}_0 = 0.24$ m/s^2, sat. E02. 32
3.12. Delay/Doppler plots, multi-frame processing, $T_{\text{int}} = 8$ s, $T_f = 0.5$ s, $\widehat{a}_{0,n} = a_{0,n}$ m/s^2, sat. E02. 33
3.13. Delay/Doppler plot, multi-frame processing, $T_{\text{int}} = 8$ s, $T_f = 0.5$ s, $\widehat{a}_{0,n} = a_{0,n}$ m/s^2, different satellites. 34

4.1. Maximum detection range comparison. 35
4.2. Multistatic processing system block diagram. 36
4.3. Multistatic geometry of interest. 37

4.4. Multistatic geometry transformation. 39
4.5. Multistatic multi-frame processing. 43
4.6. Domain transformation, noise-free, compensated, $T_{\text{int}} = 8$ s, sat. E02. . . 45
4.7. Domain transformation, noise-free, compensated, $T_{\text{int}} = 8$ s, sat. E22. . . 45
4.8. Domain transformation, noise-free, compensated, $T_{\text{int}} = 8$ s, sat. E11. . . 46
4.9. Domain transformation, noise-free, compensated, $T_{\text{int}} = 8$ s, sat. E21. . . 46
4.10. Multistatic delay/Doppler map, noise-free, compensated, $T_{\text{int}} = 8$ s, sat. E02 + sat. E22 + sat. E11 + sat. E21. 47
4.11. Domain transformation, compensated, $T_{\text{int}} = 8$ s, sat. E02. 48
4.12. Domain transformation, compensated, $T_{\text{int}} = 8$ s, sat. E22. 49
4.13. Domain transformation, compensated, $T_{\text{int}} = 8$ s, sat. E11. 49
4.14. Domain transformation, compensated, $T_{\text{int}} = 8$ s, sat. E21. 50
4.15. Multistatic delay/Doppler map, compensated, $T_{\text{int}} = 8$ s, sat. E02 + sat. E22 + sat. E11 + sat. E21. 50

B.1. Domain transformation, compensated, $T_{\text{int}} = 8$ s, sat. E15. 57
B.2. Domain transformation, compensated, $T_{\text{int}} = 8$ s, sat. E13. 57

List of Tables

2.1. E5a/E5b code parameters. 9

3.1. Link budget parameters. 21
3.2. Input signal-to-noise ratio (SNR) parameters. 21
3.3. Single frame approach SNR performance. 27
3.4. Constant acceleration multi-frame approach SNR performance. 32
3.5. Variable acceleration multi-frame approach SNR performance. 33

4.1. ξ_i overview. 42
4.2. Multistatic map peak power. 47

A.1. Parameter comparison of the different GNSS signals. 54

Bibliography

[1] ICAO. "State of global air transport and icao forecasts for effective planning". (2016), [Online]. Available: https://www.icao.int/Meetings/ICAN2017/Documents/ICAO%20Workshop%20-%20State%20of%20Industry%20and%20ICAO%20Forecasts.pdf.

[2] IATA. "Global outlook for air transport - june 2023 - report". (Jun. 2023), [Online]. Available: https://www.iata.org/en/iata-repository/publications/economic-reports/global-outlook-for-air-transport----june-2023/.

[3] Airservices Australia. "ADS-B coverage". (2021), [Online]. Available: https://www.airservices-australia.com/about-us/projects/ads-b/ads-b-coverage/ (visited on 09/26/2023).

[4] U.S. Department of Transportation Federal Aviation Administration. "Introduction to TCAS II version 7.1". (2011), [Online]. Available: https://www.faa.gov/documentLibrary/media/Advisory_Circular/TCAS%20II%20V7.1%20Intro%20booklet.pdf.

[5] EUROCONTROL. "Air traffic control surveillance coverage maps". en. (Jan. 2019), [Online]. Available: https://www.eurocontrol.int/publication/air-traffic-control-surveillance-coverage-maps (visited on 09/25/2023).

[6] F. Santi, F. Pieralice, and D. Pastina, "Joint detection and localization of vessels at sea with a GNSS-based multistatic radar", *IEEE Transactions on Geoscience and Remote Sensing*, vol. 57, no. 8, pp. 5894–5913, 2019. DOI: 10.1109/tgrs.2019.2902938.

[7] A. Filip-Dhaubhadel, "L-band Digital Aeronautical Communication System (LDACS)-Based Non-Cooperative Passive Multistatic Radar for Civil Aviation Surveillance", Ph.D. dissertation, 2019.

[8] EUROCONTROL. "Multi-Static Primary Surveillance Radar (MSPSR)." (2011), [Online]. Available: https://www.eurocontrol.int/publications/multi-static-primary-surveillance-radar-mspsr.

[9] H. Kuschel, M. Ummenhofer, P. Lombardo, F. Colone, and C. Bongioanni, "Passive radar components of Argus 3D", *IEEE Aerospace and Electronic Systems Magazine*, vol. 29, no. 3, 15–25, 2014. DOI: 10.1109/maes.2014.6805362.

[10] N. Rodriguez-Alvarez, J. F. Munoz-Martin, and M. Morris, "Latest Advances in the Global Navigation Satellite System—Reflectometry (GNSS-R) Field", en, *Remote Sensing*, vol. 15, no. 8, p. 2157, Jan. 2023, ISSN: 2072-4292. DOI: 10.3390/rs15082157. [Online]. Available: https://www.mdpi.com/2072-4292/15/8/2157 (visited on 09/04/2023).

[11] M. Antoniou and M. Cherniakov, "GNSS-based bistatic SAR: A signal processing view", *EURASIP Journal on Advances in Signal Processing*, vol. 2013, no. 1, 2013. DOI: 10.1186/1687-6180-2013-98.

[12] D. Pastina, F. Santi, F. Pieralice, M. Antoniou, and M. Cherniakov, "Passive Radar Imaging of Ship Targets With GNSS Signals of Opportunity", *IEEE Transactions on Geoscience and Remote Sensing*, vol. 59, no. 3, pp. 2627–2642, Mar. 2021, ISSN: 1558-0644.

[13] H. Ma, M. Antoniou, A. G. Stove, J. Winkel, and M. Cherniakov, "Maritime Moving Target Localization Using Passive GNSS-Based Multistatic Radar", *IEEE Transactions on Geoscience and Remote Sensing*, vol. 56, no. 8, pp. 4808–4819, Aug. 2018, ISSN: 1558-0644. DOI: 10.1109/TGRS.2018.2838682.

[14] H. Ma, M. Antoniou, D. Pastina, F. Santi, F. Pieralice, M. Bucciarelli, and M. Cherniakov, "Maritime moving target indication using passive GNSS-based bistatic radar", *IEEE Transactions on Aerospace and Electronic Systems*, vol. 54, no. 1, 115–130, 2018. DOI: 10.1109/taes.2017.2739900.

[15] D. Pastina, F. Santi, F. Pieralice, M. Bucciarelli, H. Ma, D. Tzagkas, M. Antoniou, and M. Cherniakov, "Maritime moving target long time integration for GNSS-based passive bistatic radar", *IEEE Transactions on Aerospace and Electronic Systems*, vol. 54, no. 6, pp. 3060–3083, 2018. DOI: 10.1109/taes.2018.2840298.

[16] F. Pieralice, D. Pastina, F. Santi, and M. Bucciarelli, "Multi-transmitter ship target detection technique with GNSS-based passive radar", in *International Conference on Radar Systems (Radar 2017)*, Oct. 2017, pp. 1–6. DOI: 10.1049/cp.2017.0418.

[17] Z. Li, C. Huang, Z. Sun, H. An, J. Wu, and J. Yang, "BeiDou-based passive multistatic radar maritime moving target detection technique via space–time hybrid integration processing", *IEEE Transactions on Geoscience and Remote Sensing*, vol. 60, pp. 1–13, 2022. DOI: 10.1109/tgrs.2021.3128650.

[18] X. Zhou, P. Wang, J. Chen, Z. Men, W. Liu, and H. Zeng, "A modified radon fourier transform for GNSS-based bistatic radar target detection", *IEEE Geoscience and Remote Sensing Letters*, vol. 19, pp. 1–5, 2022. DOI: 10.1109/lgrs.2020.3041623.

[19] A. Almodóvar-Hernández, D. Mata-Moya, M.-P. Jarabo-Amores, N. Rey-Maestre, and M. Benito-Ortiz, "Motion Compensation for Long Integration Times and DoA Processing in Passive Radars", en, *Remote Sensing*, vol. 15, no. 4, p. 1031, Jan. 2023, ISSN: 2072-4292. DOI: 10.3390/rs15041031. [Online]. Available: https://www.mdpi.com/2072-4292/15/4/1031 (visited on 07/24/2023).

[20] B. Wang, H. Cha, Z. Zhou, and J. Lu, "Novel Target Detection Method for GNSS_based Bistatic Radar", in *2022 Photonics & Electromagnetics Research Symposium (PIERS)*, ISSN: 1559-9450, Apr. 2022, pp. 151–154. DOI: 10.1109/PIERS55526.2022.9792777. [Online]. Available: https://ieeexplore.ieee.org/document/9792777 (visited on 09/25/2023).

[21] H.-C. Zeng, J. Chen, P.-B. Wang, W. Yang, and W. Liu, "2-D Coherent Integration Processing and Detecting of Aircrafts Using GNSS-Based Passive Radar", en, *Remote Sensing*, vol. 10, no. 7, p. 1164, Jul. 2018, ISSN: 2072-4292. DOI: 10.3390/rs10071164. [Online]. Available: https://www.mdpi.com/2072-4292/10/7/1164 (visited on 07/24/2023).

[22] T. He, L. Cui, P. Wang, and X. Zhou, "Non-Cooperative Air Target Detection Based Gnss Bistatic Passive Radar", in *IGARSS 2022 - 2022 IEEE International Geoscience and Remote Sensing Symposium*, ISSN: 2153-7003, Jul. 2022, pp. 2793–2796. DOI: 10.1109/IGARSS46834.2022.9883804.

[23] B. Wang, H. Cha, Z. Zhou, and B. Tian, "Clutter Cancellation and Long Time Integration for GNSS-Based Passive Bistatic Radar", en, *Remote Sensing*, vol. 13, no. 4, p. 701, Jan. 2021, ISSN: 2072-4292. DOI: 10.3390/rs13040701. [Online]. Available: https://www.mdpi.com/2072-4292/13/4/701 (visited on 07/24/2023).

[24] E. Kaplan and C. J. Hegarty, *Understanding GPS/GNSS : Principles and Applications, Third Edition, Principles and Applications, Third Edition*. Artech House Publishers, 2017, p. 1002, ISBN: 9781630810580.

[25] European Space Agency. "Navipedia", [Online]. Available: https://gssc.esa.int/navipedia/index.php/Main_Page.

[26] C. Günther, "Satellite Navigation Lecture Notes", Chapter 5: Signals, 2008.

[27] European Commission and Directorate-General for Internal Market, Industry, Entrepreneurship and SMEs, *European GNSS (Galileo) open service: Signal in space interface control document*. Publications Office, 2010.

[28] M. I. Skolnik, "Chapter 25: Bistatic Radar", in *Radar Handbook*. McGraw-Hill, 1990.

[29] V. S. Chernyak, *Fundamentals of Multisite Radar Systems: Multistatic Radars and Multistatic Radar Systems*. London: Routledge, Oct. 2017, ISBN: 9780203755228. DOI: 10.1201/9780203755228.

[30] E. Leon. "Generation of the ambiguity function for ultra wideband radar waveforms.", Naval Postgraduate School. (1993), [Online]. Available: https://core.ac.uk/download/pdf/36719913.pdf.

[31] M. Cherniakov, R. Saini, M. Antoniou, R. Zuo, and E. Plakidis, "Experiences gained during the development of a passive BSAR with GNSS transmitters of opportunity", *International Journal of Navigation and Observation*, vol. 2008, 1–12, 2008. DOI: 10.1155/2008/807958.

[32] Danipascual. "Danipascual/GNSS-MATLAB: MATLAB codes to generate GNSS prns, secondary codes, dataless signals and spectra. includes real data captures and a theory summary. GPS (L1CA, L2C, L5), Gaileo (E1OS, e5), Beidou-2 (B1i)", [Online]. Available: `https://github.com/danipascual/GNSS-matlab`.

[33] Z. Zeng, "Passive bistatic SAR with GNSS transmitter and a stationary receiver", Ph.D. dissertation, University of Birmingham, 2013.

[34] A. A. Ragel, "Research Internship Report", 2023.

[35] C. Moscardini, D. Petri, A. Capria, M. Conti, M. Martorella, and F. Berizzi, "Batches algorithm for passive radar: A theoretical analysis", *IEEE Transactions on Aerospace and Electronic Systems*, vol. 51, no. 2, pp. 1475–1487, Apr. 2015, ISSN: 1557-9603. DOI: `10.1109/TAES.2015.130407`.

[36] M. A. Richards, *Fundamentals of Radar Signal Processing, Third Edition*, eng, Third edition. New York, N.Y: McGraw Hill LLC, 2022, ISBN: 9781260468724 9781260468717.

[37] X. Li, G. Cui, W. Yi, L. Kong, and J. Yang, "Range migration correction for maneuvering target based on generalized keystone transform", in *2015 IEEE Radar Conference (RadarCon)*, ISSN: 2375-5318, May 2015, pp. 0095–0099. DOI: `10.1109/RADAR.2015.7130977`.

[38] Z. He, Y. Yang, and W. Chen, "A Hybrid Integration Method for Moving Target Detection With GNSS-Based Passive Radar", *IEEE Journal of Selected Topics in Applied Earth Observations and Remote Sensing*, vol. 14, pp. 1184–1193, 2021, ISSN: 2151-1535. DOI: `10.1109/JSTARS.2020.3037200`.

[39] X. Guan, L.-h. Zhong, D.-h. Hu, and C.-b. Ding, "An extended processing scheme for coherent integration and parameter estimation based on matched filtering in passive radar", en, *Journal of Zhejiang University SCIENCE C*, vol. 15, no. 11, pp. 1071–1085, Nov. 2014, ISSN: 1869-196X. DOI: `10.1631/jzus.C1400074`. [Online]. Available: `https://doi.org/10.1631/jzus.C1400074` (visited on 10/02/2023).

[40] A. Filip-Dhaubhadel and D. Shutin, "Long Coherent Integration in Passive Radar Systems Using Super-Resolution Sparse Bayesian Learning", *IEEE Transactions on Aerospace and Electronic Systems*, vol. 57, no. 1, pp. 554–572, Feb. 2021, ISSN: 1557-9603. DOI: `10.1109/TAES.2020.3026844`.

[41] D. Zhu and Z. Zhu, "Range Resampling in the Polar Format Algorithm for Spotlight SAR Image Formation Using the Chirp z -Transform", *IEEE Transactions on Signal Processing*, vol. 55, no. 3, pp. 1011–1023, Mar. 2007, ISSN: 1941-0476. DOI: `10.1109/TSP.2006.887144`.

[42] Global Positioning System Wing (GPSW) Systems Engineering & Integration, *Navstar GPS Space Segment - User Segment L1C Interfaces, Interface Specification (IS-GPS-800C)*. Washington, DC, 2013. [Online]. Available: `http://www.gps.gov/technical/icwg/`.

[43] Global Positioning System Directorate Systems Engineering & Integration, *Navstar GPS Space Segment Navigation User Segment Interfaces, Interface Specification (IS-GPS-200G)*. Washington, DC, 2013. [Online]. Available: `http://www.gps.gov/technical/icwg/`.

[44] Global Positioning System Wing (GPSW) Systems Engineering & Integration, *Navstar GPS Space Segment - User Segment L5 Interfaces, Interface Specification (IS-GPS-705C)*. Washington, DC, 2013. [Online]. Available: `http://www.gps.gov/technical/icwg/`.

[45] J. A. Avila-Rodriguez, "On Generalized Signal Waveforms for Satellite Navigation", Ph.D. dissertation, Universität der Bundeswehr, München, Neubiberg, 2000.

[46] M. Martin-Neira, S D'Addio, C Buck, N Floury, and R Prieto-Cerdeira, "The PARIS Ocean Altimeter In-Orbit Demonstrator", *IEEE Transactions on Geoscience and Remote Sensing*, vol. 49, no. 6, pp. 2209–2237, Jun. 2011, ISSN: 0196-2892. DOI: `10.1109/TGRS.2010.2092431`. [Online]. Available: `http://ieeexplore.ieee.org/lpdocs/epic03/wrapper.htm?arnumber=5682027`.